Year: 2015

Direct insights into observational absorption line analysis methods of the circumgalactic medium using cosmological simulations

Churchill, Christopher W ; Vliet, Jacob R Vander ; Trujillo-Gomez, Sebastian ; Kacprzak, Glenn G ; Klypin, Anatoly

DIRECT INSIGHTS INTO OBSERVATIONAL ABSORPTION LINE ANALYSIS METHODS OF THE CIRCUMGALACTIC MEDIUM USING COSMOLOGICAL SIMULATIONS

Christopher W. Churchill[1], Jacob R. Vander Vliet[1], Sebastian Trujillo-Gomez[1],
Glenn G. Kacprzak[2] and Anatoly Klypin[1]
Accepted to ApJ January 2015

ABSTRACT

We study the circumgalactic medium (CGM) of a $z = 0.54$ simulated dwarf galaxy using hydroART simulations. We present our analysis methods, which emulate observations, including objective absorption line detection, apparent optical depth (AOD) measurements, Voigt profile (VP) decomposition, and ionization modeling. By comparing the inferred CGM gas properties from the absorption lines directly to the gas selected by low ionization H I and Mg II, and by higher ionization C IV and O VI absorption, we examine how well observational analysis methods recover the "true" properties of CGM gas. In this dwarf galaxy, low ionization gas arises in sub-kiloparsec "cloud" structures, but high ionization gas arises in multiple extended structures spread over 100 kpc; due to complex velocity fields, highly separated structures give rise to absorption at similar velocities. We show that AOD and VP analysis fails to accurately characterize the spatial, kinematic, and thermal conditions of high ionization gas. We find that H I absorption selected gas and O VI absorption gas arise in totally distinct physical gas structures, calling into question current observational techniques employed to infer metallicities and the total mass of "warm-hot" CGM gas. We present a method to determine whether C IV and O VI absorbing gas is photo or collisionally ionized and whether the assumption of ionization equilibrium is sound. As we discuss, these and additional findings have strong implications for how accurately currently employed observational absorption line methods recover the true gas properties, and ultimately, our ability to understand the CGM and its role in galaxy evolution.

Subject headings: qalaxies: dwarf — galaxies: halos — (galaxies:) quasars: absorption lines

1. INTRODUCTION

A challenge placed before ΛCDM hydrodynamic cosmological simulations is to form realistic galaxies while matching such quantities as the stellar-mass to halo-mass relation and average star formation history as a function of halo mass and redshift (e.g., Behroozi et al. 2010, 2013; Moster et al. 2013; Munshi et al. 2013; Trujillo-Gomez et al. 2013; Ceverino et al. 2014; Agertz & Kravtsov 2014). In the simulations, the interplay between stellar feedback processes, originating in the interstellar medium (ISM), and filamentary and galaxy accretion, originating in the intergalactic medium (IGM), give rise to extended metal-enriched gaseous structures surrounding galaxies, i.e., the circumgalactic medium (CGM). The exact role of the CGM in governing the observed properties of galaxies is not yet well established; however, it is quite possible that the CGM is a highly regulating component of galaxies and, if better understood, could provide powerful insights into global galaxy relations (cf., Oppenheimer et al. 2010; Mathes et al. 2014)

Thus, it is an additional challenge for successful simulations to also statistically match the observed distributions of gas density, temperature, kinematics, and chemical and ionization conditions of the CGM. In general, there are two main approaches to simulating galaxies and the CGM. The first uses smoothed particles hydrodynamics (SPH), which discretizes gas mass into particles, and the second uses adaptive mesh refinement (AMR), which spatially discretizes the gas using grid cells.

SPH simulations generally trade off high spatial and mass resolution in favor of modeling the hydrodynamics in thousands of galaxies in a simulation box. A great strength of SPH simulations is that the statistical characteristics of the CGM can be studied over a wide range of halo mass and cosmological environment. The draw back is that the detailed physics of stellar formation and feedback are generally in the form of scaling relations, such as constant velocity winds, or winds with launch velocities proportional to the stellar velocity dispersion, which scales with the gravitational potential (e.g. Oppenheimer & Davé 2008; van de Voort & Schaye 2012). These relations do not directly address the underlying physics of feedback.

A strength of AMR simulations is that the star formation and feedback models directly target the underlying physical processes of star formation and feedback. Though the processes are still unresolved, the physics is highly detailed and the simulations can be employed to study star formation at the scale of molecular cloud physics and stellar feedback at the scale of radiation pressure physics and photo-heating physics (Trujillo-Gomez et al. 2013; Ceverino et al. 2014; Agertz & Kravtsov 2014). With such detail, the draw back is that only a few galaxies can be simulated at a time. However, with AMR, greater insight into the complex interplay between star formation and feedback that regulates the CGM, and therefore galaxy formation and evolution, can be gleaned.

Observationally, the primary method for studying the gas properties of the CGM is the technique of quasar absorption lines. The most commonly studied CGM absorption lines are H I $\lambda 1215$ (Lyα) and H I $\lambda 1025$ (Lyβ) (e.g., Lanzetta et al. 1995; Stocke et al. 2013; Tumlinson et al. 2013; Mathes et al. 2014), the lithium isosequence zero-volt resonant doublets C IV $\lambda\lambda 1548, 1550$ and O VI $\lambda\lambda 1031, 1037$ (e.g., Simcoe et al.

[1] New Mexico State University, MSC 4500, Las Cruces, NM 88003, USA
[2] Centre for Astrophysics and Supercomputing, Swinburne University of Technology, PO Box 218, Victoria 3122, Australia

2006; Stocke et al. 2006; Fox et al. 2007a,b; Tumlinson et al. 2011; Stocke et al. 2013; Mathes et al. 2014), and the sodium isosequence zero-volt resonant doublet Mg II $\lambda\lambda 2796, 2803$ (e.g., Nielsen et al. 2013a,b, and references therein). Virtually all of the physical conditions we have learned about the CGM are derived from absorption line analysis. As such, studying the CGM properties of simulated galaxies and quantitatively comparing these properties to those derived from observations is clearly best accomplished using absorption line measurement and analysis methods (also see Ford et al. 2013a,b; Hummels et al. 2013).

Absorption line analysis of simulations will not only directly increase our knowledge of the CGM and its role in galaxy evolution, but will provide a profound insight into how effective and accurate commonly applied observational analysis methods recover the "true" gas properties (densities, temperatures, chemical and ionization conditions, and kinematics). To accomplish these objectives, we must quantitatively compare the inferred gas properties derived from observational techniques applied to synthetic absorption lines in simulations directly to the physical properties of the simulation gas from which the absorption arises.

For example, ionization models (e.g., Cloudy, Ferland et al. 1998, 2013) are used to determine the gas density, $n_{\rm H}$, and metallicity, as well as the ionization parameter, $U = n_\gamma/n_{\rm H}$, where n_γ is the number density of hydrogen ionizing photons. Many assumptions are invoked in applying these models, such as single-phase absorbing clouds (e.g., Churchill et al. 2012; Lehner et al. 2013; Stocke et al. 2013; Fox et al. 2014; Werk et al. 2014), or simple two-phase absorbing clouds (e.g., Churchill & Charlton 1999; Charlton et al. 2003; Ding et al. 2003; Tripp et al. 2011; Kacprzak et al. 2012). How appropriate are these assumptions? Quantifying the relationships between absorption profiles, the inferred properties of the absorbing gas from the absorption line data, and the true" properties of the gas giving rise to the absorption in the simulations can provide insight to this question.

A second example is the inferred kinematics, which is either assumed to be provided by the profile of the column density with velocity via the apparent optical depth (AOD) column density method (e.g., Savage & Sembach 1991), or reflected in Voigt profile (VP) decomposition of the absorption profile (e.g., Boksenberg et al. 1979; Churchill et al. 2003b; Simcoe et al. 2006; Mathes et al. 2014). However, inferring the properties of the gas using either the AOD profile method and VP decomposition implicitly relies on the assumption that gas at a given velocity arises from a single unique spatial location along the line of sight. Furthermore, VP decomposition models the data as isothermal clouds, each having a different peculiar velocity. Using simulations, the relative spatial locations of the absorbing gas along the LOS can be examined to quantify the degree to which absorption with similar (or aligned) kinematics arises in the same spatial gas structures. This latter information has important implications for the assumptions applied to the ionization modeling and kinematic analysis of observed data.

To be effective, the application of absorption line analysis to simulations should emulate observational work as closely as possible so that the selection methods, spectral resolution, sensitivity limitations, and analysis techniques of various absorption-line surveys can be accurately duplicated. In general, surveys target a limited number of absorption line transitions, each which probe a relatively narrow range of gas phase, i.e., they arise in gas with favorable density, temperature, ionization conditions, and metallicities. This will also be true for absorption lines in synthetic spectra obtained by passing sightlines through the CGM in hydrodynamic simulations. For example, along a single sightline, some gas structures may contribute to Mg II and/or C IV absorption, whereas other unique gas structures may contribute to O VI absorption, but not to Mg II or C IV absorption.

But, importantly, all our knowledge of the CGM from absorption line analysis is filtered through the instruments that modify the data. Which instrument and telescope facility is used to observe a given absorption line depends upon the rest wavelength of the transition and the redshift of the absorbing structure, and this strongly governs the design, sensitivity, and data quality for observational surveys. Since which absorption lines get observed depend upon which facilities capture the wavelength range of the redshifted transition, this governs which gas phases can be probed and to what level of sensitivity they can be probed.

Furthermore, the range of physical gas properties that contribute to detectable absorption will differ as a function of the detection thresholds of the spectra, which depends on the signal-to-noise ratio, resolution, and pixelization of the data. Shallower detection thresholds result in probing gas with higher column densities, which presumably means that higher density, higher metallicity gas, or favorable ionization conditions are preferentially being studied. This holds true for both real-world observations and synthetic spectra from simulations, provided that the synthetic spectra are carefully designed to emulate real-world spectra.

With the aforementioned considerations in mind, in this paper we describe the methods we developed to generate "realistic" synthetic spectra through simulated galaxies in AMR cosmological simulations and to analyze the spectra, all in a manner that emulates real-world observations. In Section 2 we describe the simulated galaxy we employ for this study. In Section 3, we briefly review the ionization model (Churchill et al. 2014) used to obtain the gas ionization conditions. We detail our methods for absorption line analysis in Section 4 and discuss selected preliminary findings in Section 5. In Section 6, we summarize our work.

2. THE SIMULATIONS

We employ the N-body plus gasdynamics AMR code hydroART (Kravtsov et al. 1997; Kravtsov 1999; Kravtsov & Klypin 1999; Kravtsov et al. 2004). The simulations were run using the "zoom-in" technique (Klypin et al. 2001), which allows us to resolve the formation of a single galaxy consistently in its full cosmological context. The high-resolution region around the galaxy is typically ~ 1–2 Mpc across and the hydrodynamics is resolved with 7×10^6 grid cells, with a minimum cell size of roughly 30 h^{-1} pc at $z = 0$ (the proper size of the cells decrease with increasing redshift).

Physical processes implemented in the code include star formation, stellar feedback, Type II and Ia metal enrichment, thermal and radiation pressure, and metallicity-dependent cooling and heating. Gas is self-shielded, advects metals, is heated by a homogeneous ultraviolet background, and can cool to 300 K due to metal and molecular line cooling. Gas flows, shock fronts, and metal disbursement follow self-consistently from this physics.

For star formation, we use observations of molecular clouds (Krumholz & Tan 2007) to guide our model. The star par-
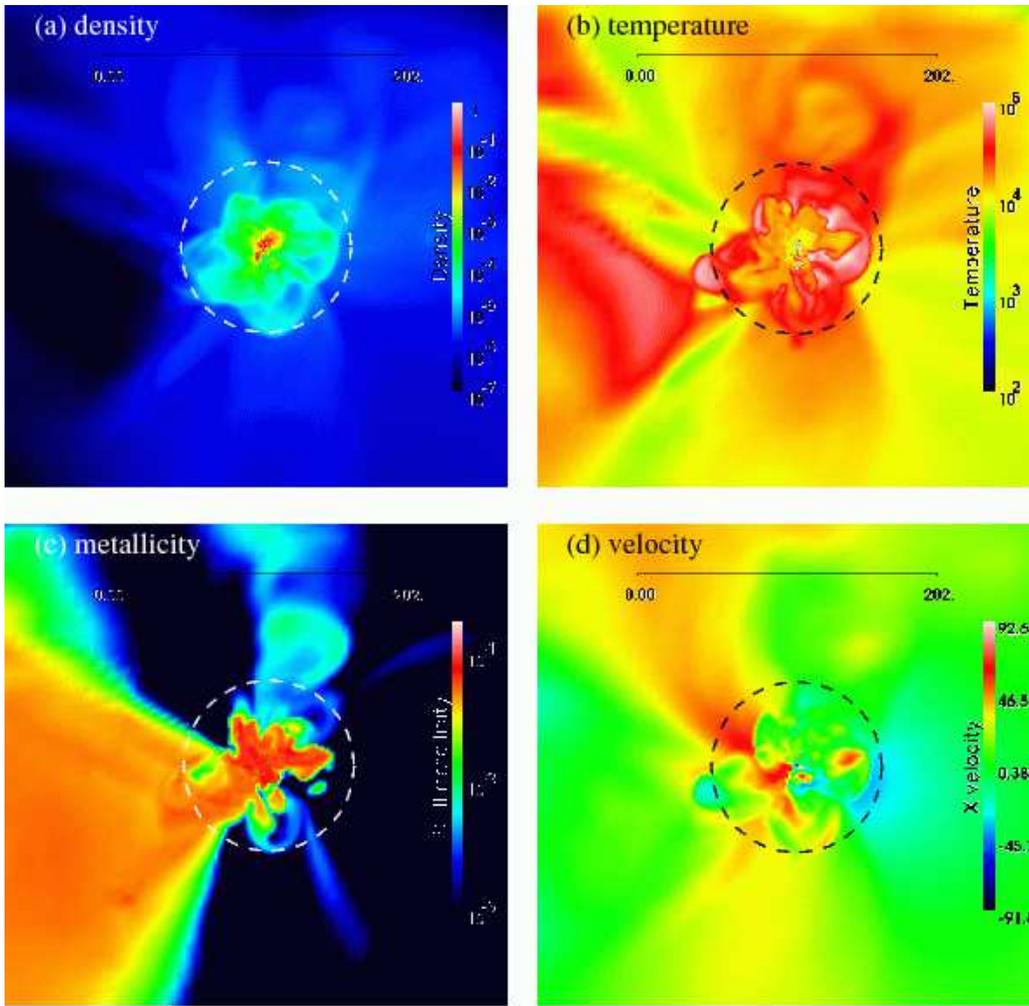
Figure 1. Slices centered on the center of mass of a $z = 0.54$ simulated galaxy for the dwALL_8 feedback model of Trujillo-Gomez et al. (2013), showing the gas (a) number density, (b) temperature, (c) Type II supernovae metal mass fraction yield, and (d) x-component of the velocity (where the x direction is positive to the right). The horizontal bar across each panel provides the physical scale in proper kiloparsecs and the dashed circles show the virial radius. The dwALL_8 star formation and feedback model includes deterministic star formation in molecular cloud environments, supernova heating, stellar winds, radiation pressure, and photo-heating. At $z = 0.54$, the galaxy has virial mass $M_{\mathrm{vir}} = 2.7 \times 10^{10}$ M$_\odot$, virial radius $R_{\mathrm{vir}} = 57$ kpc, and stellar mass $M_* = 1.2 \times 10^7$ M$_\odot$.

ticles form in the dense, cold molecular phase ($n_{\mathrm{H}} \sim 100$ cm^{-3}, $T \simeq 100$ K). The star formation rate is proportional to the gas density divided by the free fall time of the molecular cloud. We use an observationally motivated low (2% percent) efficiency per free fall time for converting gas into stars. Compared to previous methods (Ceverino & Klypin 2009; Ceverino et al. 2010), this treatment results in a greater number of individual star particles, but with smaller masses, between ~ 100 and $\sim 10^3$ M$_\odot$. Runaway young, hot stars are included according to Ceverino & Klypin (2009) by providing one third of the newly-formed star particles with a random velocity kick.

For the feedback model, mechanical energy from stellar winds and SN type II is assumed to thermalize and is injected into the gas as thermal energy around young stars following the rates predicted by Starburst99 (Leitherer et al. 1999) for the Chabrier IMF (Chabrier 2003). We also incorporated photoionization heating, radiation pressure, and shocked stellar winds from massive stars (see Ceverino & Klypin 2009; Ceverino et al. 2010; Trujillo-Gomez et al. 2013; Ceverino et al. 2014, for details). These feedback processes disrupt the cold molecular gas and

regulate the formation of stars (Trujillo-Gomez et al. 2013; Ceverino et al. 2014).

Matching observations of HII regions (Lopez et al. 2014), we treat photoheating by adding a non-thermal pressure ($P/k \simeq 10^6$ K cm^{-3}) to the gas surrounding young stars. This pressure decreases rapidly in order to reproduce the declining density within a growing HII region. For radiation pressure, which we treat similarly to Murray & Rahman (2010), (Hopkins et al. 2011), and Agertz et al. (2013), we include momentum from the radiation field from young massive, which is coupled to the gas and dust through scattering and absorption. Absorption of UV photons scales as $1 - e^{-\tau_{\mathrm{UV}}} \simeq 1$. Scattering due to trapped IR photon scales as $\tau_{\mathrm{IR}} \simeq 1$. These values are adopted from the suggested values of (Krumholz & Thompson 2012) based upon τ_{IR} scaling with column density (Davis et al. 2014).

This star formation and feedback model was shown to reproduce many properties of low-mass galaxies at $z \sim 0$ without fine tuning (see Trujillo-Gomez et al. 2013); the stellar to halo mass ratio, cold gas fraction, baryon content, star formation history, rotation curves and morphologies of the simulated galaxies agree remarkably well with observations.

The heating and cooling balance of the gas is determined using heating and cooling functions obtained from Cloudy (Ferland et al. 1998, 2013) and incorporates equilibrium photoionization and collisional ionization. These include metal and molecular line cooling, and a uniform Haardt & Madau (2001) ionizing background with self-shielding of high column density gas, and stellar radiation for gas in the vicinity of stars. For additional details see Ceverino et al. (2010).

At each grid cell, the hydroART code follows the evolution of the density, temperature, velocity, and metal mass fraction. The metals produced in type II and Ia supernovae are followed separately and are self-consistently advected with the gas flow. To compute the relative abundances of the ions in the gas, we employ an equilibrium ionization model as a postprocessing step. We briefly describe the ionization model in Section 3; full details are given in Churchill et al. (2014).

For the analysis in this paper, we adopt the simulation of the low-mass (dwarf) galaxy designated dwALL_8 presented in Trujillo-Gomez et al. (2013). For this simulation, the host dark matter halo evolved into an isolated dwarf galaxy with a virial mass $M_{\mathrm{vir}} = 2.8 \times 10^{10}$ M$_\odot$, a virial radius $R_{\mathrm{vir}} = 80$ kpc, a stellar mass $M_* = 2.1 \times 10^7$ M$_\odot$, and a maximum circular velocity $v_c = 60$ km s^{-1} at $z = 0$. As described above, the dwALL_8 model incorporates feedback in which the optical depth of the gas and dust to IR photons is small and the pressure of the gas due to photo-heating in H II regions is $P/k = 8 \times 10^6$ K cm^{-3}. These assumptions are within the range favored by observations of star forming regions. The dark matter particle resolution is 9.4×10^4 M$_\odot$.

We study the galaxy when it is at redshift $z = 0.54$. At this redshift, the galaxy has virial mass $M_{\mathrm{vir}} = 2.7 \times 10^{10}$ M$_\odot$, virial radius $R_{\mathrm{vir}} = 57$ kpc, and stellar mass $M_* = 2.1 \times 10^7$ M$_\odot$. In the galaxy interstellar medium, the minimum gas cell proper size is 27 h^{-1} pc. In the circumgalactic medium, the proper cell sizes range from 27 h^{-1} pc to 432 h^{-1} pc. Within two virial radii, there are $\sim 7 \times 10^6$ gas cells.

In Figure 1, we present thin slices through the gas distribution centered on the galaxy at $z = 0.54$, showing (a) gas density, (b) temperature, (c) metallicity, and (d) the x-component of velocity. The scale is indicated in physical kpc at the top of each panel and the dashed circles show the virial radius.

3. THE IONIZATION MODEL

We developed an ionization model specifically designed for post-processing application with the hydroART cosmological simulations. The details of the code, including comparisons with the industry standard ionization code Cloudy (Ferland et al. 1998, 2013) are presented in Churchill et al. (2014). The code has also been successfully applied for observational work (e.g., Kacprzak et al. 2012; Churchill et al. 2012). Here, we briefly summarize the ionization modeling of the gas in the simulations.

For each individual gas cell in the simulation box, the ionization model calculates the equilibrium ionization state of the gas. The ionization model treats photoionization, Auger ionization, direct collisional ionization, excitation auto-ionization processes, charge exchange ionization, radiative recombination, dielectronic recombination, and charge exchange recombination. If desired, the effects of each of these processes can be isolated by turning the process "off" or "on". The output of the ionization code is a simulation box containing the cell equilibrium electron densities, and the number densities of all ions. We thus have the ability to study

the spatial distribution of the ions. If desired, the photoionization rates and recombination and collisional ionization rate coefficients in a given cell can be recorded for specified ions.

Three cell properties constrain the gas physics (1) the total hydrogen density of the cell, n_{H}, (2) the equilibrium temperature of the cell, T, and (3) the mass fractions of the atomic species in the cell, which is given as the type II and Ia supernovae yields from the stellar feedback and metal transport. Metals up to and including zinc are incorporated into the ionization model. The fourth quantity that governs the gas physics is the spectral energy distribution of ionizing photons. The ionization model accounts for the ultraviolet background (UVB), and/or radiation from the stellar particles (populations) in the simulated galaxy.

3.1. *Optically Thin Constraint*

A limitation of the current version of the ionization model is that only optically thin gas can be treated because we presently do not treat radiative transfer through the grid cells[3]. As discussed in Churchill et al. (2014), we employ the definition for "optically thin" to mean that the optical depth is less than unity at the hydrogen and helium ionization edges, which dominate modification of the ionizing SED. We showed that the cloud models are constrained to have upper limits on the column densities of $N_{\mathrm{HI}} = 1.58 \times 10^{17}$ cm^{-2} for neutral hydrogen, $N_{\mathrm{HeI}} = 2.77 \times 10^{17}$ cm^{-2} for neutral helium, and $N_{\mathrm{HeII}} = 6.34 \times 10^{17}$ cm^{-2} for singly ionized helium.

Via the relationship $L = N_{\mathrm{Xj}}/f_{\mathrm{Xj}} n_{\mathrm{X}}$, where N_{Xj} is the column density of atomic species X in ionization stage j, f_{Xj} is the ionization fraction of ion X^j, and n_{X} is the number density of species X, the upper limits on column density translate into upper limits on the cell size, $L_{\max}$, for validity of the optically thin constraint. In Churchill et al. (2014), we showed that the cell size upper limits can be written,

$$
\begin{aligned}
L_{\max}(\mathrm{H\,I}) &\simeq 0.5 \cdot (0.01/f_{\mathrm{HI}})(0.01/n_{\mathrm{H}}) \\
L_{\max}(\mathrm{He\,I}) &\simeq 9 \cdot (0.01/f_{\mathrm{HeI}})(0.01/n_{\mathrm{H}}) \quad \mathrm{kpc} \quad (1) \\
L_{\max}(\mathrm{He\,II}) &\simeq 20 \cdot (0.01/f_{\mathrm{HeII}})(0.01/n_{\mathrm{H}}) \;,
\end{aligned}
$$

assuming a relative abundance of helium to hydrogen of 10%.

The proper minimum cell size for the simulations at $z = 0.54$ (the redshift of the galaxy we study in this work) is $\simeq 0.03$ kpc. From Eq. 1, we see that only in cases where the product of the ionization fraction and the hydrogen number density exceed 10^{-4} does the maximum cell size decrease from the fiducial values of 0.5, 9, and 20 kpc for the respective ionization edges. In Churchill et al. (2014), we further showed that the maximum allowed cell size is below the 30 pc resolution minimum for $\log n_{\mathrm{H}} \geq -2.2$ when $3 \leq \log T \leq 4$, and for $\log n_{\mathrm{H}} \geq -1.2$ when $\log T \simeq 5$. For $\log T \geq 5.5$, the maximum allowed cell size is never less than 30 pc. As such, our ionization model is currently not entirely valid for "cold" cells ($\log T < 4$) with densities $\log n_{\mathrm{H}} > -2$ nor for "warm/hot" cells ($\log T \simeq 5$) with densities $\log n_{\mathrm{H}} > -1$. The former cells are found to reside almost exclusively in the ISM of the simulated dwarf galaxies, and the latter cells are virtually non-existent because the warm/hot gas is associated with densities in the range $\log n_{\mathrm{H}} < -1$.

3.2. *Comparison with Cloudy*

---

[3] We are currently developing the techniques to account for shielding effects.

Direct comparisons between our ionization model and Cloudy 13.03 (Ferland et al. 2013) showed that the two codes are in good agreement (Churchill et al. 2014). The ionization fractions of neutral hydrogen are virtually identical over the density and temperature ranges $-7 \leq \log n_H \leq +1$ and $2 \leq \log T \leq 7$. The helium ionization fractions are also in full agreement except for a factor of 2-3 overestimate for neutral helium for $\log T > 5$. Comparison of the ionization corrections, $\log f_{X^j}/f_{HI}$, were in agreement within ± 0.05 for the commonly observed ions Mg^+, C^{+3}, and O^{+5} over the majority of the $\log n_H$–T parameter space. Most importantly, as we discuss Churchill et al. (2014), the region of agreement is always within $\log f_{X^j}/f_{HI} \leq 0.05$ where the ionization fractions of the target ions are the largest, meaning that dominant ionization stages where absorption will be most affected are in agreement with Cloudy. Given that $\log N_{X^j} \propto \log f_{X^j}/f_{HI}$, we argued that since typical uncertainties in observed column density measurements range between ± 0.05 to ± 0.1 in the logarithm, the difference in the ionization corrections between the two ionization models would be consistent with typical measurement errors in $\log N_{X^j}$ obtained from absorption line analysis.

4. ABSORPTION LINE ANALYSIS OF THE CGM

4.1. *The Simulation Box and Sightlines*

The redshift of the simulation box is denoted z_{box}. The position of the center of the galaxy in the box, $\mathbf{x}_g = (x_{1g}, x_{2g}, x_{3g})$, is obtained by locating the center of mass of the stellar particles surrounding the minimum of the gravitational potential. The peculiar velocity of the galaxy in the box is the velocity of the center of mass of the stellar particles, and is denoted $\mathbf{v}_g = (\dot{x}_{1g}, \dot{x}_{2g}, \dot{x}_{3g})$.

First, the ionization model is run on the simulation box, from which the number densities of all ions are determined for each gas cell. To generate "observed" quasar spectra (see Section 4.2), a line of sight (LOS) is passed through the simulation box from the vantage point of an "observer" viewing the galaxy on the plane of the sky. Each LOS is defined by (1) an impact parameter, D, (2) a position angle on the plane of the sky, Φ, which ranges from $\Phi = 0°$ to $360°$, and (3) the inclination, i, of the simulated galaxy with respect to the LOS direction.

The orientation of the galaxy in the simulation box is defined by the angular momentum vector of the star particles. Once D, Φ, and i are specified, we determine the direction cosines (ℓ, m, n) of the LOS with respect to the box coordinate system. For an individual simulated galaxy, we can create and study an arbitrary number of randomly oriented or parallel LOS. This formalism allows the opportunity study the relationship between galaxy orientation and absorption line properties (e.g., Bordoloi et al. 2011; Bouché et al. 2012; Kacprzak et al. 2012; Mathes et al. 2014).

The position along the LOS for cell i is

$$\Delta S_i = \left[\ell(x_{1i} - x_{1g})^2 + m(x_{2i} - x_{2g})^2 + n(x_{3i} - x_{3g})^2 \right]^{1/2}, \quad (2)$$

where $\mathbf{x}_i = (x_{1i}, x_{2i}, x_{3i})$, measured in kiloparsecs, is the position of cell i intercepted by the LOS. The plane of the sky is defined as the plane perpendicular to the LOS intersecting $\Delta S = 0$. Since the LOS unit vector is $\hat{\mathbf{s}} = \ell \hat{\mathbf{i}} + m \hat{\mathbf{j}} + n \hat{\mathbf{k}}$, the cell LOS velocity with respect to the simulation box is $v_i = \hat{\mathbf{s}} \cdot \mathbf{v}_i$, where $\mathbf{v}_i = (\dot{x}_{1i}, \dot{x}_{2i}, \dot{x}_{3i})$ is the cell velocity vector, and the observed redshift of the cell is $z_i = z_{box} + (v_i/c)(1 + z_{box})$. The LOS systemic velocity of the galaxy is $v_g = \hat{\mathbf{s}} \cdot \mathbf{v}_g$, and the "observed" redshift of the galaxy is $z_g = z_{box} + (v_g/c)(1 + z_{box})$.

The column density of ion X^j for each cell along the LOS is $N_{X^j,i} = n_{X^j,i} L_i = f_{X^j,i} n_{X,i} L_i$, the product of the number density of the ion in the cell and the pathlength of the LOS through the cell, L_i, which is the true length of the LOS vector through the cell computed as the pathlength from the entry to the exit points on the cell walls.

For this investigation, we ran 1000 LOS through the simulated galaxy from the perspective of a face-on orientation. The LOS range from $0 \leq D \leq 90$ kpc, corresponding to $0 \leq D/R_{vir} \leq 1.5$. In Figure 2 (lower set of panels), we illustrate selected cell physical quantities as a function of the LOS position, ΔS, over the range $-65 \leq \Delta S \leq 65$ kpc (corresponding to $R \simeq R_{vir} \simeq 1$) for LOS 0092 through the simulated galaxy shown in Figure 1. This LOS is at $D = 11$ kpc, which corresponds to $D/R_{vir} = 0.2$. We selected this particular LOS for illustration purposes because it gives rise to both low ionization and high ionization absorption, and therefore provides insights to both gas phases. Overall, LOS 0092 is typical of the many LOS that probe the simulated galaxy in the range $0.1 \leq D/R_{vir} \leq 0.4$.

From top to bottom in Figure 2, we present the gas cell hydrogen number density, $\log n_{i\,H}$, temperature, $\log T_i$, gas-phase metallicity[4], $\log Z_i/Z_\odot$, line of sight velocity, $\Delta v_i = v_i - v_g$, and ion column density, $\log N_{X^j,i}$. The curves are presented as histograms that show the gas cell pathlengths along the LOS. Recall that $\Delta S = 0$ is the plane of the sky (defined by the galaxy center).

Multiple panels of each property are repeated from left to right in Figure 2 in order to illustrate which cells contribute to detected absorption for the H I Lyβ, Mg II $\lambda\lambda 2796, 2803$, C IV $\lambda\lambda 1548, 1550$, and O VI $\lambda\lambda 1031, 1037$ transitions (we discuss how these cells are determined in Section 4.4). The synthetic absorption lines are shown in the top set of panels (generation of the synthetic spectra is described in Section 4.2). These absorbing cells are marked with $\times$ points overplotted on the histograms (see Section 5.2 for further discussion).

For this LOS, the CGM of the simulated dwarf has density range $-5 \leq \log n_H \leq -1.5$, temperature range $4.2 \leq \log T \leq 4.6$, and metallicity range $-3.5 \leq \log Z/Z_\odot \leq -2$. Positive temperature spikes of ~ 0.3 dex occur in regions of ~ 0.5–1 dex reductions in density. From the behavior of the LOS velocity, there is a clear outflow for $\Delta S > 0$ kpc, with a velocity inversion in the range $+10 \leq \Delta S > +20$ kpc, which is characterized by a drop in density and increase in temperature. Note the ~ 0.5 dex drop in metallicity at $\Delta S = +15$ kpc that proceeds the velocity inversion. Visual inspection of density, temperature, metallicity, and velocity slices of the simulated galaxy shown in Figure 1 clearly show that the CGM of this galaxy is as highly variable, dynamic, and complex as this single LOS example indicates.

The computation of the cell column densities (bottom panels of Figure 2) rely on the ionization modeling. Based upon our criteria for optically thin gas as determined by the optical depth at the hydrogen and helium ionization edges, we find that even in the cells where the H^0 and Mg^+ column densities are highly peaked, only one gas cell along the LOS barely violates the optically thin criteria. Note that the C^{+3} and O^{+5} column densities have a relatively flat distribution along the LOS out to $\Delta S \sim \pm 50$ kpc.

---

[4] $Z/Z_\odot = (x_M/x_H)/(x_M/x_H)_\odot$, where x_M is the mass fraction of all metals and x_H is the mass fraction of hydrogen.
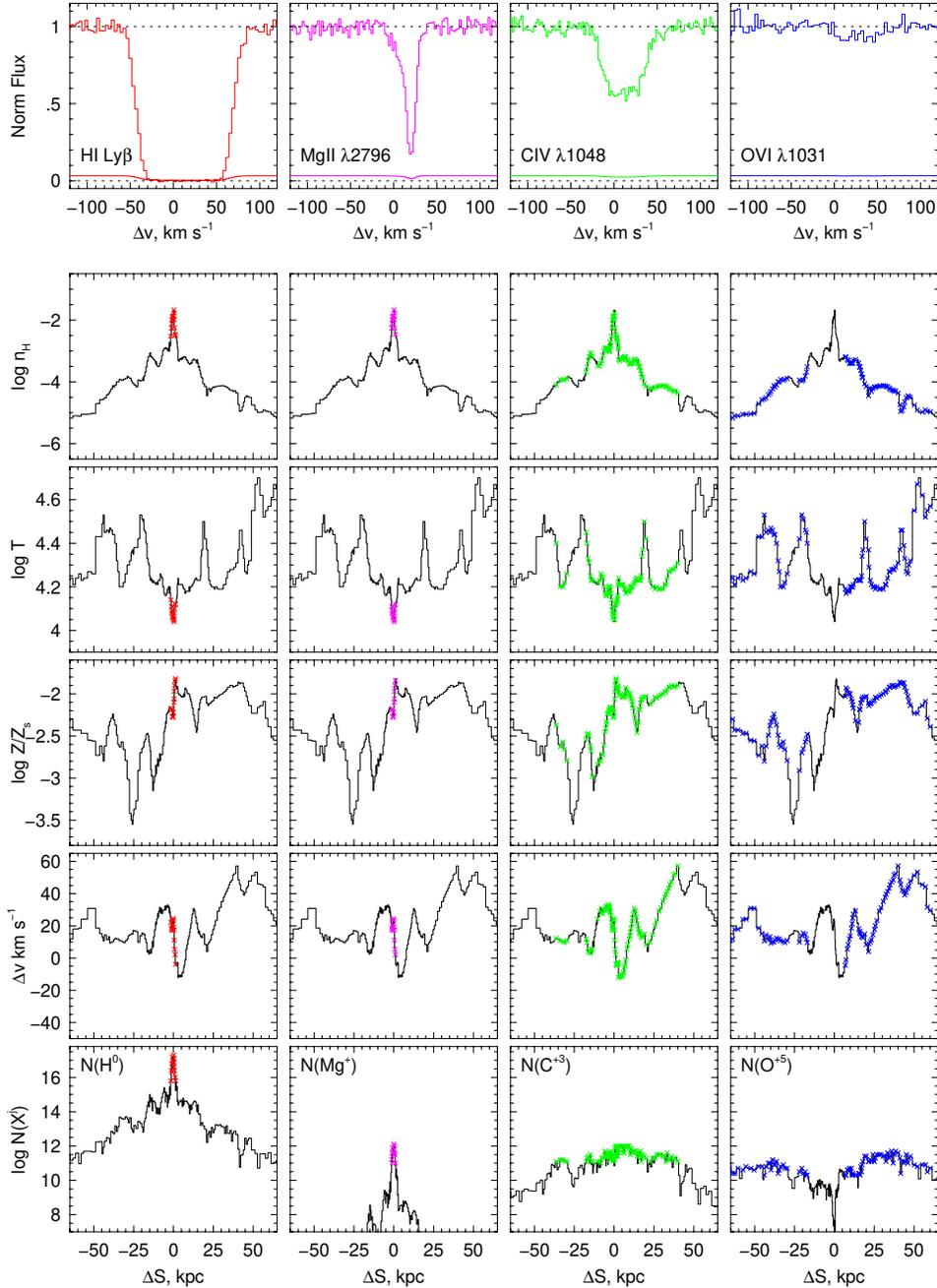
Figure 2. Selected "observed" absorption profiles and gas cell properties for a line of sight through the simulated galaxy (LOS 0092). (upper panel) Absorption profiles determined from Eqs. 3–11 (*HST*/COS for *SNR* = 30) as a function of velocity relative to galaxy systemic, for the neutral hydrogen Ly β transition the blue transitions of the zero-volt resonant doublets for the Mg⁺, C⁺³, and O⁺⁵ ions. (lower panels, from top to bottom) Gas cell hydrogen number density, $\log n_H$, temperature, $\log T$, metallicity, $\log Z/Z_\odot$, line of sight velocity, Δv, and ion column density, $\log N_{xj}$, as a function of line of sight position ΔS. The sightline is perpendicular to the plane of the sky, and the zero point, $\Delta S = 0$, corresponds to the plane of the sky defined by the galaxy center. The cell column densities are determined from the ionization modeling. Note that even though the absorption profiles are closely aligned in velocity space, the absorption is arising in physically distinct regions along the line of sight.

4.2. *Generation of Simulated Spectra*

The simulated absorption spectra are generated with our code Specsynth with the assumption that each cell, i, contributes to the optical depth as if it were an isothermal "cloud". For a given transition from ion X^j, the optical depth as a function of observed wavelength is computed from

$$\tau_i(\lambda) = N_{x^j,i} \frac{\sqrt{\pi}e^2}{m_e c^2} \frac{f\lambda_0^2}{\Delta\lambda_i} U(a,b), \tag{3}$$

where the physical constants have their usual meaning, λ_0 is the rest-frame wavelength of the transition, f is the transition oscillator strength, and $N_{x^j,i}$ is the column density of the ion. The term

$$\Delta\lambda_i = \frac{\lambda_0}{c} \left\{ \frac{2kT_i}{m_x} \right\}^{1/2} \tag{4}$$

is the Doppler width, where m_x is the mass of the ionic species. The Voigt function, $U(a,b)$, is computed as the real
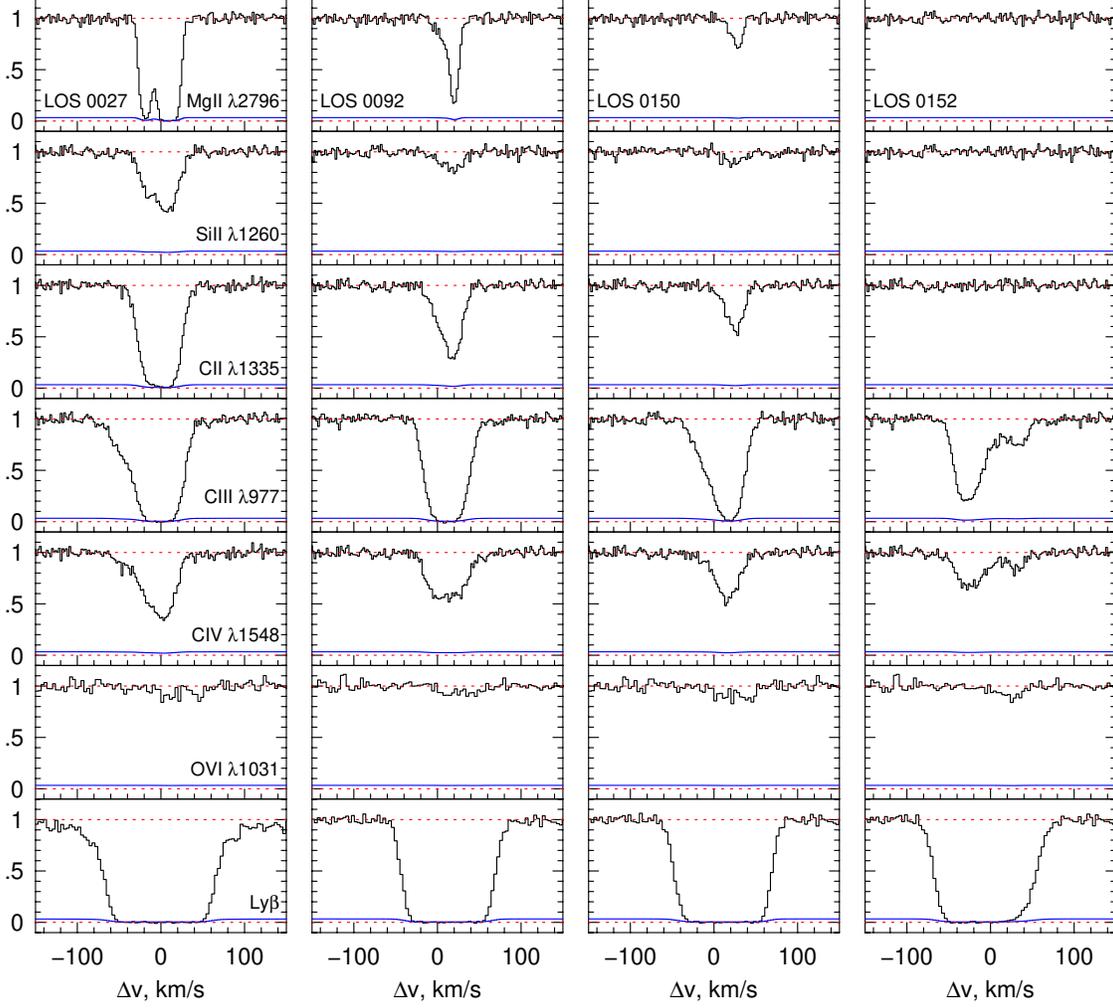
Figure 3. Selected synthetic absorption profiles for four LOS through the simulated galaxy. From left to right, the LOS are 0027, 0092, 0150, and 0152, with increasing impact parameter range from $D \simeq 9$ to 30 kpc ($D/R_{\rm vir} \simeq 0.15$ to 0.5). The profiles and LOS properties for LOS 0092 (second from the left) have been further illustrated in Figure 2. The spectra have resolution have $SNR = 30$, and correspond to the HIRES and COS FUV and NUV gratings.

part of the complex probability function using the code Cpf12 (Humlíček 1979) with unitless parameters

$$a = \frac{1}{\Delta\lambda_i} \frac{\lambda - \lambda_c}{(1 + z_g)}, \quad b = \frac{1}{\Delta\lambda_i} \frac{\Gamma\lambda_0^2}{4\pi c}, \tag{5}$$

where the factor $1 + z_g$ ensures that the wavelength difference, $\lambda - \lambda_c$, is co–moving corrected, and where $\lambda_c = \lambda_0(1 + z_i)$ is the redshifted central wavelength of the absorbing cell. The resulting normalized counts in the spectrum prior to being recorded by an instrument are obtained by

$$\mathcal{I}'(\lambda) = \prod_{i=1}^{N_c} \exp[-\tau_i(\lambda)], \tag{6}$$

where N_c is the number of cells along the LOS.

The spectrum is then "passed through" an instrument. The choice of instrument would be dictated by which ions and redshifts are being studied so that the spectra can be directly comparable to observational data. For example, H I Lyman series lines and the O VI doublet at low redshifts, i.e., $z < 0.3$, are observed in COS G130M spectra, whereas the Mg II doublet at $z > 0.3$ is studied in Keck/LRIS, Keck/HIRES and/or

VLT/UVES spectra. Having chosen an instrument, we first convolve $\mathcal{I}'(\lambda)$ with the instrument spread function (ISF), $\Phi(\lambda' - \lambda)$, yielding the instrument convolved normalized spectrum,

$$\mathcal{I}(\lambda) = \Phi(\lambda' - \lambda) * \mathcal{I}'(\lambda'). \tag{7}$$

The convolved normalized spectrum is then sampled with the pixelization $\Delta\lambda_{\rm pix}$, of the chosen instrument. Finally, Gaussian deviate noise is added on a pixel by pixel basis assuming a fixed signal-to-noise ratio per pixel, SNR, and adopting the instrumental read noise, RN. The read noise is applied in units of electrons, and not in digital number (which is smaller by the readout amplifier gain factor) because properly modeling the Poisson statistics requires electron counts. The adopted SNR ideally should be selected to reflect the average SNR of the observed spectra comprising surveys targeting the transition being studied in the simulations. In this way, the detection sensitivities of observational surveys are emulated for a direct comparison between spectra from simulations and real world spectra.

The normalized uncertainty spectrum due to Poisson statis-

tics is given by

$$\sigma_{\mathcal{I}}(\lambda) = \frac{\left[\mathcal{I}_c \mathcal{I}(\lambda) + RN^2\right]^{1/2}}{\mathcal{I}_c}, \tag{8}$$

where

$$\mathcal{I}_c = \frac{(SNR)^2}{2}\left[1 + \sqrt{1 + 4\left(\frac{RN}{SNR}\right)^2}\right] \tag{9}$$

approximates the continuum counts for the desired *SNR* (Churchill 1997). To account for the additional uncertainty due to placement of the continuum fit (as required for observational spectra), we adopt an approximation that the uncertainty due to continuum placement is proportional to the Poissonian uncertainty in the continuum, i.e., $h\,\sigma_{\mathcal{I}_c}(\lambda)$, where $\mathcal{I}(\lambda) = 1$ (see Sembach & Savage 1992). The final normalized uncertainty spectrum is then

$$\sigma(\lambda) = \sqrt{\sigma_{\mathcal{I}}^2(\lambda) + h^2 \sigma_{\mathcal{I}_c}^2(\lambda)}$$
$$= \frac{\sqrt{\mathcal{I}_c \mathcal{I}(\lambda) + RN^2 + h^2\left[\mathcal{I}_c + RN^2\right]}}{\mathcal{I}_c}, \tag{10}$$

To determine the proportionality constant, h, we undertook a blind experiment. We generated 100 synthetic spectra from several common instruments with a range of *SNR* (from 5 to 50) and added continuum shapes ranging from from 2nd order to 7th order Legendre polynomials. Each spectrum had 2048 pixels. We then interactively continuum fit the spectra and computed the mean standard deviation (over all pixels) between the noiseless input continua and the blindly fitted smooth continua. This yielded $h = 0.4$, which, in continuum regions, corresponds to an 8% increase for the final uncertainty relative to the Poisson-only uncertainty.

The final pixelated normalized spectrum with noise is computed from

$$I(\lambda) = \mathcal{I}(\lambda) + G_{pix}\sigma(\lambda), \tag{11}$$

where G_{pix} is a random unit Gaussian deviate generated on a per pixel basis.

For each LOS (and there can be an arbitrary number per simulated galaxy), an individual synthetic spectrum and uncertainty spectrum is generated for each ion/transition that we aim to study. The observed wavelength range of a given synthetic spectrum is set such that the spectrum covers $\Delta v = \pm 1000$ km s^{-1} with respect to the system velocity of the simulated galaxy. However, this range can be adjusted and redefined with ease.

In Figure 3, we present example synthetic spectra for four LOS (0027, 0092, 0150, and 0152, from left to right in order of increasing impact parameter) through the the simulated galaxy shown in Figure 1. The impact parameter range from $D \simeq 9$ to 30 kpc ($D/R_{vir} \simeq 0.15$ to 0.5). From top to bottom, we show the the commonly studied Mg II $\lambda2796$, Si II $\lambda1260$, C II $\lambda1335$, C III $\lambda977$, C IV $\lambda1548$, O VI $\lambda1031$ transitions, and the H I Ly β transition. For this example, we adopt *SNR* = 30 per pixel and show only the "blue" member of the doublets.

Since the simulated galaxy is at $z = 0.54$, the Mg II lines are redshifted into the optical at 4306 Å so we adopt the HIRES instrument ($R = 45,000$) for this doublet. We model the HIRES ISF as a unit-area Gaussian with $\sigma = c/2.35R = 2.83$ km s^{-1}, corresponding to 3 pixels per resolution element

(6.6 km s^{-1}). The Ly β, O VI and C III lines are observed in the FUV G160M grating of COS ($R \simeq 20,000$), the C II and C IV lines are observed in the NUV G225M grating of COS ($R \simeq 22,000$), and the Si II line is observed with the NUV G185M grating of COS ($R \simeq 18,000$). For the COS ISFs we employ the on-line Lifetime Position 2 tabulated theoretical line spread functions (Kriss 2011). We determine the ISF at a given observed wavelength using cubic spline interpolation.

LOS 0092 (second from left) is the LOS illustrated in Figure 2. Note that as impact parameter is increased the low ionization absorption diminishes and the C III and C IV absorption develops somewhat greater kinematic complexity. We further discuss the nature of the absorption for LOS 0092 in Section 5.

4.3. *Analysis of Simulated Spectra*

In order to emulate observational analysis common to quasar absorption line studies, we adopt objective methods used (or that should be used) for observed spectra. We use a fully automated version of our graphical interactive code Sysanal, which we have applied for several other works (e.g., Churchill & Vogt 2001; Evans 2008; Churchill et al. 2012; Kacprzak et al. 2012; Evans et al. 2013; Mathes et al. 2014). After all measured quantities are calculated, the final step of the process is the generation of a single table for each ion that contains the absorption properties for all LOS. These tables can then be analyzed to study the CGM properties of the simulated galaxies.

4.3.1. *Objective Absorption Line Detection*

To locate statistically significant absorption features in the synthetic spectra, we employ the methods described in Churchill et al. (1999) and Churchill et al. (2000), which are derived from Schneider et al. (1993).

First, the spectrum is converted to an equivalent width spectrum, $w(\lambda)$, and the uncertainty spectrum is converted to an equivalent width uncertainty spectrum, $\sigma_w(\lambda)$. The equivalent width spectrum provides the observed (not rest-frame) equivalent width per resolution element for an unresolved absorption feature as a function of observed wavelength and the equivalent width uncertainty spectrum provides the 1 σ observed equivalent width detection threshold as a function of observed wavelength. The computation of $w(\lambda)$ and $\sigma_w(\lambda)$ requires convolving the normalized and pixelized ISF with the flux decrements in each pixel of the spectrum (see Section 3.1.1 and Equations 1 and 2 of Churchill et al. 2000).

An absorption feature is objectively defined in spectral regions where $w(\lambda) \leq -N\sigma_w(\lambda)$, where we adopt $N = 5$ for singlet absorption lines. For doublets, we adopt $N = 5$ for the blue (higher oscillator strength) member of a doublet and $N = 3$ for the red member of a doublet. For a doublet to be "detected", both members must satisfy the above detection criteria. However, to facilitate direct comparison with observational data from various surveys that may adopt different criteria, the detection criteria can easily be tailored to those of any survey.

The lower and upper wavelength limits over which the absorption feature is defined are taken to be where $w(\lambda) \geq -1\sigma_w(\lambda)$ is first recovered while scanning the spectrum blueward and then redward of the wavelength first satisfying the detection criterion. Using this method, several "sub-features", absorption separated by continuum, can be uniquely defined and analyzed (see Figure 1 of Churchill & Vogt 2001).

In Figure 4, we illustrate the detection method for objectively defining absorption features. In the upper panels, we
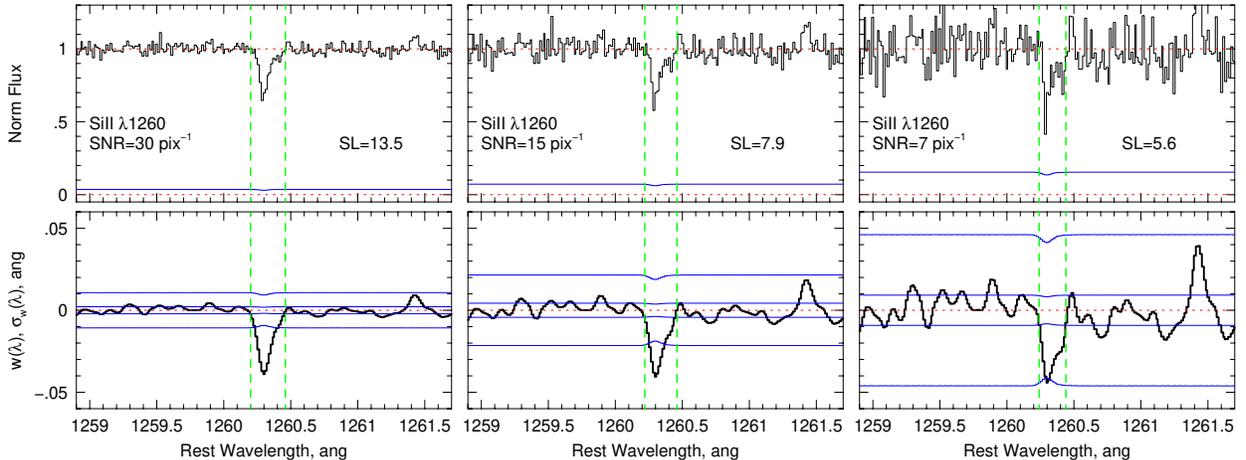
Figure 4. Detection method and criteria for objectively defining absorption features. (top panels) De-redshifted Si II λ1260 absorption (COS G185M/1621B) for three *SNR* values (left) *SNR* = 30, (center) *SNR* = 15, (right) *SNR* = 7 per pixel. The blue spectrum provides the 1 σ uncertainty in the normalized flux. (bottom panels) The rest-frame equivalent width per resolution element, $w(\lambda)$. The bracketing blue spectra are the $\pm 1\sigma_w(\lambda)$ and $\pm 5\sigma_w(\lambda)$ equivalent width detection thresholds for unresolved absorption lines, where $\sigma_w(\lambda)$ is the equivalent width uncertainty spectrum. An absorption feature is detected at wavelength λ when $w(\lambda) \leq -5\sigma_w(\lambda)$. The spectral range of the absorption feature (green vertical lines) is defined at the wavelengths where $w(\lambda) \leq -\sigma_w$ is first recovered, i.e., $w(\lambda)$ becomes consistent with $\sigma_w(\lambda)$. For each realization of the absorption line , the detection significance level, *SL* is provided, where $SL = W_r/\sigma_{W_r}$.

present the rest-frame Si II λ1260 synthetic absorption lines for the COS G185M/1921 grating for Stripe B. We vary the *SNR* values (left) *SNR* = 30, (center) *SNR* = 15, (right) *SNR* = 7 per pixel. The blue spectrum provides the 1 σ uncertainty in the normalized flux. In the lower panels of Figure 4, we present the rest-frame equivalent width spectrum, $w(\lambda)$. We also present the $\pm 1\sigma_w(\lambda)$ and $\pm 5\sigma_w(\lambda)$ rest-frame equivalent width detection thresholds for unresolved absorption lines as the bracketing blue spectra. Note that the 5 σ detection threshold changes from $\simeq 0.011$ Å for *SNR* = 30 to $\simeq 0.045$ Å for *SNR* = 7. For *SNR* = 30 and 15, several pixels across the profiles are clearly significant at greater than the 5 σ level. However, for *SNR* = 7, the absorption feature is on the verge of detection; had the noise characteristics been different, this feature may not have been formally detected. The green vertical lines mark the wavelength range over which the absorption profiles are defined for the purpose of quantifying the absorption.

Sysanal works simultaneously on all ion/transitions for a given LOS. Once all synthetic spectra for a LOS are objectively searched for absorption features, and the spectral ranges of the detected absorption features are determined, the code then computes the observed and rest-frame equivalent widths, doublet ratios (when applicable), the flux decrement weighted velocity centers, velocity widths, and velocity asymmetries. Formal uncertainties in these quantities are also computed.

In the case of nondetections, the 3 σ upper limits are computed for the observed and rest-frame equivalent widths. In the case where multiple sub-features are detected, they are individually measured in addition to the measurement of the "total system" quantities (all sub-features treated as a single absorption feature). The mathematical computation of these quantities, originally based on the work of Sembach & Savage (1992), is given in Churchill (1997) and in the Appendix of Churchill & Vogt (2001). Additional details are provided in Sections 3.1–3.4 of Evans (2008).

4.3.2. *Apparent Optical Depth Spectra*

Sysanal also creates an apparent optical depth (AOD) column density spectrum and uncertainty AOD spectrum for each ion/transition (Savage & Sembach 1991). From these spectra, we determine the "best" AOD column density spectrum for a given ion. For ions with multiple transitions, such as H I and the common metal-line doublets, we employ the following procedure. For a given velocity pixel, we take the optimal weighted mean AOD column density of the transitions if (1) more than one transition for a given ion has measured values (not lower or upper limits) of the AOD column density, and (2) unresolved saturation (see Savage & Sembach 1991) is not present. The uncertainties are propagated in the standard fashion. If all but one transition yields a limit, the transitions with measured values are adopted. In the case of unresolved saturation, the adopted AOD column density is taken to be that with the highest oscillator strength. In the case of upper limits in all transitions, the highest oscillator strength transition is adopted, and in the case of lower limits in all transitions, the lowest oscillator strength transition is adopted. This process yields the AOD column density profile for a given ion, $N_a(X_i; \Delta v)$ [atoms cm^{-2} (km s^{-1})$^{-1}$], from which we compute the integrated AOD column densities, $N_a(X^j)$ for each ion,

$$N_a(X^j) = \int_{\Delta v^{(-)}}^{\Delta v^{(+)}} N_a(X^j; \Delta v)\, d(\Delta v) \quad \text{atoms cm}^{-2}, \qquad (12)$$

where the integration is over the spectral region over which the absorption profile is detected (see the vertical green lines in Figure 4). If saturation persists over a minimum of three adjacent pixels, i.e., $N_a(X^j; \Delta v)$ is a lower limit over an extended velocity range approaching a resolution element, we quote a 3 σ lower limit for $N_a(X^j)$. We discuss comparison of the AOD spectra to the simulation gas properties in Section 5.2.

4.3.3. *Voigt Profile Decomposition*

The final spectral analysis step is VP decomposition, which yields the column densities, *N*, Doppler *b* parameters, and observed redshifts, *z*, of multiple VP components. To obtain

an initial model for each ion, we run Autovp[5] on the spectra. Redshifted transitions from different ions can fall in wavelength ranges appropriate for different spectrograph/grating combinations (i.e., COS, HIRES, LRIS, etc.), so that different transitions from a single LOS are likely to be measured with different resolutions. We properly account for the ISF appropriate for the instrument with which a given synthetic absorption line was created.

Due to the different kinematics of the lower and higher ionization gas, we have found that fully automating the VP decomposition of the synthetic spectra to be challenging and we are still developing our approach. Currently, we run Autovp on the lower ionization profiles and select the profile with the largest number of VP components as the initial kinematic template for the low ionization transitions. We repeat the process for the higher ionization transitions.

To obtain the final model, we then run our minimization code Minfit (Churchill 1997; Churchill & Vogt 2001; Churchill et al. 2003b). Minfit refines the model using the maximum likelihood modification of the Levenberg-Marquardt algorithm Dnls1 (More 1978), which minimizes the sum of the squares of M nonlinear functions in N variables[6]. We adopt the model with the fewest VP components that are statistically significant at the 97% confidence level by applying an F-test on the χ^2 distribution. Components with the largest fraction errors,

$$f_{\mathrm{err}} = \sqrt{\left(\frac{dN}{N}\right)^2 + \left(\frac{db}{b}\right)^2 + \left(\frac{dz}{z}\right)^2}, \qquad (13)$$

are tested for significance in descending order of f_{err}. If a component is not significant, it is removed from the model, and the process is repeated until all components are significant.

Full details of the most up-to-date version of Minfit and the fitting process are described in Evans (2008). The difference for our application is that we adopt a unique VP model for the lower ionization gas and for the higher ionization gas. Though not perfect as a description of the complex multiphase gas structures that give rise to the absorption lines, it does provide us a formalism for segregating the absorption into two gas phases. Further development is under way.

In Figure 5, we show an example of VP decomposition for LOS 0092. This is the LOS illustrated in Figure 2. For this LOS, the lower ionization species are taken to be Mg II, Si II, C II, and H I (shown as the blue fits), whereas the higher ionization species are taken to be C III, C IV, and O VI (shown as the red fits). The individual VP components are shown as magenta (except for H I Ly β, where, for clarity, one component is magenta and the second is green). The LOS velocities of the low ionization VP components are tied together and all lower ionization transitions are fitted simultaneously. The same holds for the higher ionization transitions. We assume purely thermal line broadening for each VP component. In this mode, the component temperatures are the actual fitting parameters, from which the b parameters are computed from $b_{\mathrm{xj}} = \sqrt{2kT/m_{\mathrm{x}}}$ for ion X^{j}, where n_{x} is the mass of ion X.

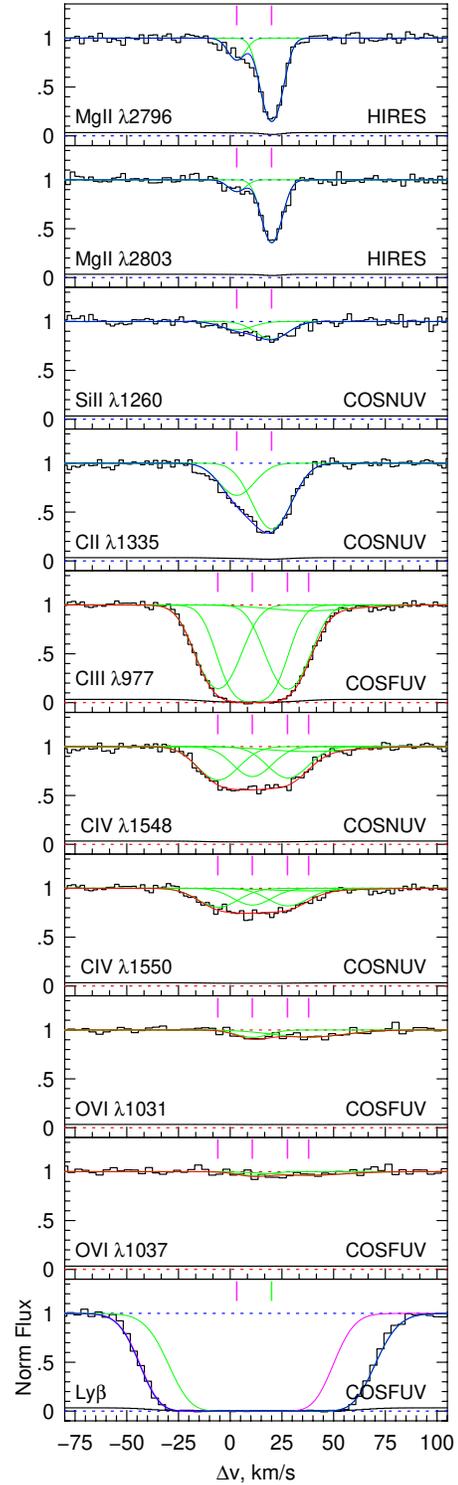For reference, we list the VP component parameters in Ta-

Figure 5. Voigt profile decomposition of selected transitions for the absorption profiles for LOS 0092 shown in Figure 2. The lower-ionization transitions of Mg II, Si II, C II, and H I (blue curves) were fitted simultaneously and separate to the higher-ionization transitions of C III, C IV, and O VI (red curves). Magenta and green curves provide the individual compoents. Though component velocities are tied between ions, the column densities and allowed to vary freely. The b parameters of each component are tied between ions through thermal scaling. The ticks above the continua provide the number of components and their velocity centroids. The instruments assumed for generation of the synthetic spectra and therefore the ISFs used in the VP decomposition are given in the lower right of each panel.

[5] Autovp was originally written R. Davé. We modified the program to incorporate convolution with the ISF.

[6] Dnls1 is part of the Slatec package publicly available at the Netlib Repository (*http://www.netlib.org*) sponsored by The University of Tennessee and the Oak Ridge National Laboratory.

Table 1
VP Decomposition of LOS 0092

(1)	(2)[a]	(3)[b]	(4)[c]	(5)
Ion/	Δv	$\log N$	b	$\log T$
Transition	(km s^{-1})	(cm^{-2})	(km s^{-1})	(K)
		Low Ionization Phase		
H I	3.20	16.27 ± 0.15	20.80 ± 0.85	4.42 ± 0.04
	20.01	16.04 ± 0.06	23.92 ± 0.46	4.54 ± 0.02
Mg II	3.20	11.77 ± 0.03	4.24 ± 0.17	4.42 ± 0.03
$\lambda\lambda 2796, 2803$	20.01	12.73 ± 0.01	4.87 ± 0.09	4.54 ± 0.02
Si II	3.20	11.72 ± 0.07	3.94 ± 0.16	4.42 ± 0.04
$\lambda 1260$	20.01	12.10 ± 0.04	4.53 ± 0.09	4.54 ± 0.02
C II	3.20	13.31 ± 0.02	6.03 ± 0.25	4.42 ± 0.04
$\lambda 1335$	20.01	13.86 ± 0.02	6.93 ± 0.13	4.54 ± 0.02
		High Ionization Phase		
C III	-5.89	13.41 ± 0.15	9.33 ± 0.76	4.80 ± 0.04
$\lambda 977$	10.69	14.66 ± 1.42	8.09 ± 4.89	4.68 ± 0.26
	27.80	13.42 ± 0.18	9.01 ± 1.05	4.77 ± 0.05
	38.05	12.19 ± 0.62	26.33 ± 8.60	5.70 ± 0.31
C IV	-5.89	13.13 ± 0.09	9.33 ± 0.76	4.80 ± 0.04
$\lambda\lambda 1548, 1550$	10.69	13.05 ± 0.23	8.09 ± 4.89	4.68 ± 0.26
	27.80	13.09 ± 0.11	9.01 ± 1.05	4.77 ± 0.05
	38.05	12.52 ± 0.61	26.33 ± 8.60	5.70 ± 0.31
O VI	-5.89	< 11.36	$\cdots$	$\cdots$
$\lambda\lambda 1031, 1027$	10.69	12.62 ± 0.56	7.01 ± 4.24	4.68 ± 0.26
	27.80	< 11.31	$\cdots$	$\cdots$
	38.05	12.95 ± 0.63	22.81 ± 6.12	5.70 ± 0.31

[a] The velocities of the components are tied together for each phase.
[b] The column densities vary freely from ion to ion.
[c] The Doppler parameters are tied via thermal broadening for each phase.

ble 1. Presented are (1) the ion and transition fitted, (2) the LOS velocity, Δv, (3) the column density, $\log N$, (4) the Doppler b parameter, and (5) the temperature. Upper limits are quoted at the $3\,\sigma$ level. We discuss comparison of the VP fit parameters to the simulation gas properties along this LOS in Section 5.2.

4.4. *Locating "Absorbing" Cells*

One of our aims is to develop methods to directly compare the "true" properties of the simulated CGM to those inferred from observations. Comparisons of the simulated CGM and the observed CGM must account for the gas being probed by the absorption lines. Isolating the gas that is responsible for detected absorption allows for *direct* comparison between the measured "observed" quantities from synthetic absorption line analysis and the physical properties of the gas. As such, it is centrally important to identify which grid cells along a given LOS are "detected" in simulated absorption lines.

In order to isolated the cells that contribute to the absorption profile from a given ion, we adopt a differencing technique. For a given ion, the cells with LOS velocities aligned within the objectively defined velocity range of the absorption profiles are sorted into descending column density order. An identification number for each cell from the simulation box is included in the list. For a given ion, we then iteratively regenerate synthetic spectra for the transition with the largest oscillator strength by progressively omitting one gas cell at a time until the equivalent width of the profile stops changing by a defined percent difference. The spectra for this exercise are appropriately convolved with the instrumental spread

function and pixelated according to the selected spectrograph and grating settings; however, the test spectra are noiseless. After testing various percent differences, we adopted 5% difference.

To elaborate, we start with the highest column density cell in the velocity range of the absorption profile, remove the cell, and recompute the profile. If the equivalent width is reduced by more than a 5% difference, $|\Delta W_r/W_r| \geq 0.05$, we consider this cell to contribute significantly to the absorption. We then advance to the next highest column density cell, regenerate the profile, and determine if the equivalent width has decreased by more than 5% difference. We repeat the process on successively smaller column density cells until the change in the equivalent width is less than a 5% difference. The result is that we identify all cells that contribute more than a 5% difference to the equivalent width of the profile. Cells that reside in the velocity range of the absorption deemed to not contribute to absorption typically have column densities a factor of 50 to 100 below the cell contributing the highest column density.

Referring back to Figure 2, we overplotted colored data points showing the properties of the absorption selected gas as a function of LOS position, ΔS. As can be seen, the H I and Mg II absorption lines arise in many of the same cells within close proximity of $\Delta S \sim 0$. The C IV absorption also arises in these cells; but the vast majority of the C IV absorbing cells are distributed over $\Delta S = \pm 40$ kpc, a region over which the gas phases change substantially along the LOS with a 2 dex variation in n_H and 0.4 dex variation in T. Note the cells at $\Delta S \simeq -25$ kpc, where $\log Z/Z_\odot$ dips below -3, do not contribute to C IV absorption (nor O VI absorption). Many of the cells that give rise to C IV absorption also give rise to O VI absorption, however, the physical extent of O VI absorbing cells along the LOS is greater than that of the C IV absorbing cells.

5. DISCUSSION

Following the methods described in Sections 4.1 and 4.2, we ran 1000 random LOS through the simulated galaxy (face-on orientation) and generated synthetic absorption line spectra of H I Lyα and Lyβ, Si II $\lambda\lambda 1190, 1193$, Si II $\lambda 1260$, C II $\lambda 1036$ and $\lambda 1335$, Mg II $\lambda\lambda 2796, 2803$, C IV $\lambda\lambda 1548, 1550$, and O VI $\lambda\lambda 1031, 1037$ transitions. The synthetic spectra have $SNR = 30$ and the characteristics of the HIRES instrument and the appropriate COS NUV or FUV high resolution gratings for a $z \simeq 0.54$ absorption line system. The $5\,\sigma$ rest-frame detection threshold of these spectra is ~ 0.01 Å (see Figure 4). The impact parameters of the LOS cover the range $0 \leq D/R_{\rm vir} \leq 1.5$, corresponding to random sky coverage within a projected separation from the galaxy of $D = 90$ kpc.

We then analyzed the absorption line spectra, measuring their equivalent widths, velocity widths, and column densities, etc., as described in Section 4.3. Finally, we determined which cells contributed to absorption following the methods described in Section 4.4.

5.1. *Phase Space of the CGM*

In Figure 6, we plot the phase diagrams (hydrogen density, n_H, versus temperature, T) showing the relative number of cells giving rise to detected absorption in the synthetic spectra for the four ions, H^0 (H I), Mg$^+$ (Mg II), C^{+3} (C IV), and O^{+5} (O VI). For these phase diagrams, we include only cells that partake in absorption lines having equivalent widths greater than 0.1 Å. This threshold is typical of the sensi-
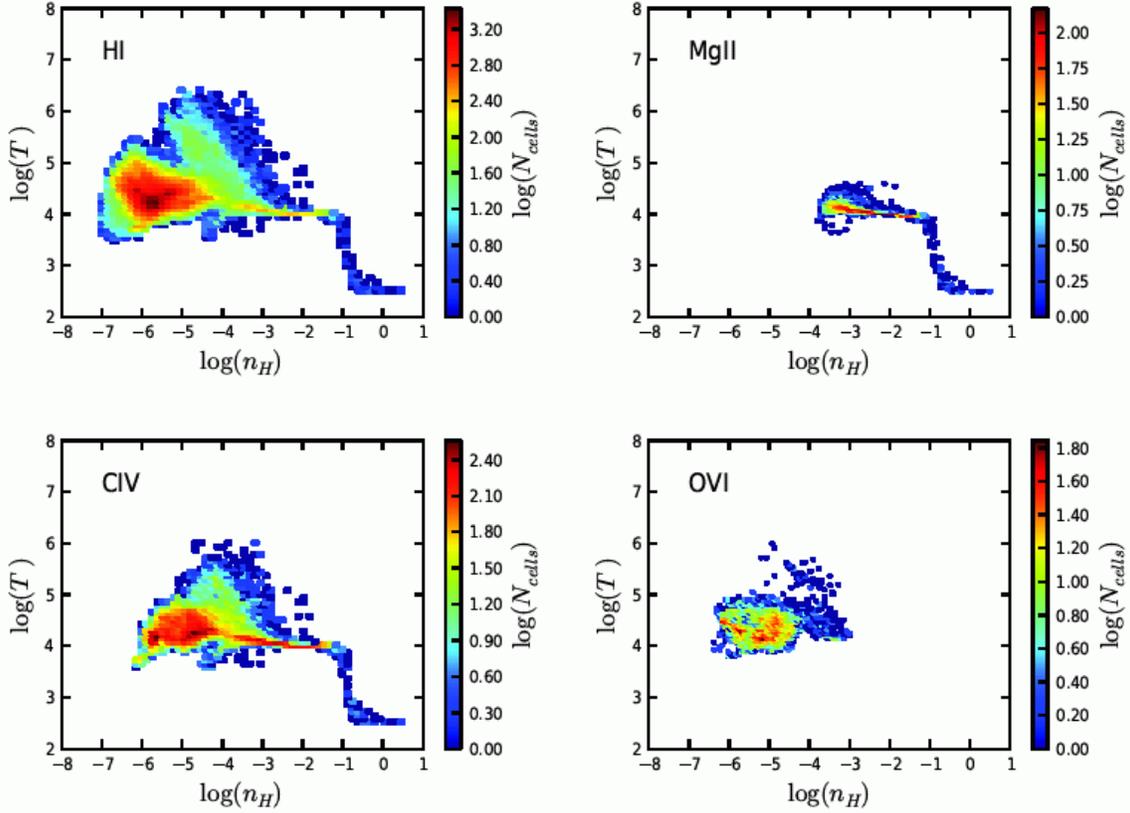
Figure 6. The phase diagrams (hydrogen density, $n_{\rm H}$, versus temperature, T) showing the relative number of cells giving rise to detected absorption in the synthetic spectra for the four ions, H I, Mg II, C IV, and O VI. These cells were selected using the criteria described in Section 4.4 for 1000 random LOS distributed within $D \leq 1.5 R_{\rm vir}$ through the simulated galaxy shown in Figure 1. The synthetic spectra have the characteristics of the appropriate COS NUV or FUV high resolution gratings for a $z \simeq 0.5$ absorption line system. The signal-to-noise ratio is 30 per pixel. We applied a $5\,\sigma$ equivalent width detection threshold of $\simeq 0.1$ Å to these spectra. Cells with gas phases in the range $\log n_{\rm H} \geq -1$ and $\log T \leq 3.8$ are from the galaxy ISM; the remaining cells are from the galaxy CGM.

tivity threshold of the COS-Halos and COS-Dwarfs surveys (Tumlinson et al. 2011, 2013; Bordoloi et al. 2014), though some of the sightlines in the surveys have deeper detection thresholds.

For H I, Mg II, and C IV, the absorbing cells with phases in the range $\log n_{\rm H} \geq -1$ and $\log T \leq 3.8$ are located in the galaxy ISM (roughly within $D/R_{\rm vir} < 0.1$); the remaining cells are located in the CGM. There is no O VI absorption from the ISM, only from the CGM. We note that the phase properties of many of the absorbing cells in the ISM do not satisfy our optically thin criteria and should be viewed with caution, whereas all cells in the CGM do meet the criteria.

For this simulated dwarf galaxy, we see that the majority of the CGM, as selected by absorption with greater than 0.1 Å, is characterized by temperatures in the range $4 \leq \log T \leq 5$; the absorbing gas is primarily what we might call the "cool/warm" CGM. Interestingly, the gas that gives rise to O VI absorption also resides in this temperature range. It would seem that the CGM of this dwarf galaxy is primarily photoionized gas (in Section 5.3, we quantify this and also discuss the appropriateness of the assumption of equilibrium ionization modeling). A minority of the absorbing cells have $\log T > 5$, and it is possible that these cells are dominated by collisional ionization processes.

The densities of the Mg II absorbing gas reside in the range $-3.5 \leq \log n_{\rm H} \leq -1.5$ and the temperatures are confined to a narrow range at $\log T \simeq 4$. Note that a substantial fraction of

the C IV absorbing cells also reside in this temperature range. However, the majority of the C IV and O VI absorbing gas primarily has lower densities in the range $-6 \leq \log n_{\rm H} \leq -4$.

The relative population of absorbing cells in phase space is such that H I and C IV absorption is selecting out significantly more cells than Mg II and O VI absorption. To the degree to which the CGM of this simulated dwarf galaxy reflects that of real-world dwarf galaxies, this would immediately suggest the observed covering fraction for H I and C IV absorption in dwarfs should be substantially higher than the covering fraction for Mg II and O VI absorption. Indeed, the covering fraction of C IV absorption for $L < 0.2L^*$ galaxies in the COS-Dwarfs sample is greater than 40% for $D/R_{\rm vir} \leq 0.5$ for a detection threshold of ~ 0.1 Å (Bordoloi et al. 2014). We defer study of how the covering fractions and the equivalent width and column density impact parameter distributions respond to different feedback recipes for future work (Vander Vliet et al. 2014a, in preparation).

The absorbing gas phase distributions for this simulated dwarf galaxy show some similarities and some differences with those obtained by Ford et al. (2013a,b), who present H I, Mg II, and C IV absorption phase diagrams for a $z = 0.25$ simulated galaxy with a halo mass of 10^{12} M$_\odot$. Their simulations are performed with SPH, whereas we have used AMR simulations.

For H I and Mg II, our absorbing gas phase distributions, obtained for 1000 LOS with $D < 90$ kpc, are qualitatively con-

sistent with the phase distributions for the LOS with $D = 100$ kpc and $D = 1$ Mpc from Ford et al. (2013a). This is likely because the overdensity of the CGM within $D = 100$ kpc in a dwarf galaxy halo is similar to that of a 10^{12} M$_\odot$ halo at $100 < D \leq 1000$ kpc. For C IV, the temperature distribution for our dwarf is similar to that found by Ford et al. (2013a), however, the distribution of n_H in the CGM of our dwarf galaxy peaks at $n_H \sim 10^{-5}$ cm^{-2}, whereas the peak found by Ford et al. (2013a) is $n_H \sim 10^{-4}$ cm^{-2} for $100 < D \leq 1000$ kpc, and is $n_H \sim 10^{-3}$ cm^{-2} for $D = 10$ kpc. We cannot compare O VI because Ford et al. (2013a) did not present a n_H–T phase diagram for this ion.

5.2. *Kinematic and Spatial Relationships*

Here, we present insights into the application of observational analysis techniques by examining the kinematic and spatial relationship between the absorption profiles and the CGM gas giving rise to absorption in simulations. For our discussion, we again focus on the H I, Mg II, C IV, and O VI absorption for LOS 0092.

Of foremost interest (also see Figure 2) is that, whereas the H I absorption-selected cells are coincident with the Mg II absorbing cells, these cells represent 15% of the C IV selected cells and none of the cells selected by O VI absorption. This non-coincidence of H I and O VI absorption-selected gas would not be perceptible in real-world observations. Since some of the H I absorption has LOS velocities coincident with the O VI absorption, it is likely that when employing common observational analysis methods some fraction of the H I column density would be attributed to the O VI absorbing gas phase (what fraction depends upon a somewhat subjective educated estimate or "artfully" modeling of the absorption, such as VP decomposition). Therefore, it is almost assured that the metallicity of the O VI absorbing phase would then be underestimated in observational studies.

This would suggest that there may be systematic bias in the metallicity determinations derived from observed O VI systems that exhibit low-ionization absorption conditions, since the H I column density might arise only within the low-ionization phase. Note that, to a large degree, the same argument holds for the C IV absorption, for which the majority of the absorbing cells are not selected by H I absorption. In their SPH simulations, Oppenheimer & Davé (2009) also find that H I and O VI absorption does not trace the same baryons, even though they are both present in the CGM. They also conclude that, if true, ths could result in underestimatations of the true metallicity, since $\log Z/Z_\odot \propto (N_{OVI}/N_{HI})(f_{HI}/f_{OVI})$.

It is possible that the lack of coincident H I and O VI absorbing gas could be a resolution effect in AMR simulations (and SPH simulations). In low density regions, where the grid-cell sizes are larger, thermal and dynamic instabilities leading to condensations of cooler higher density gas cannot be resolved. Thus, multiphase structures that might form embedded in the hotter lower density regions of the simulated CGM would be suppressed. Such structures may have been detected observationally (Crighton et al. 2014). H I and Mg II absorption arise exclusively in cells with lengths of ~ 3 kpc, where as C IV and O VI arise in cells with lengths ranging from 3–11 kpc and 6–45 kpc, respectively. Even in these extended cells, the ionization fraction of H I is so small that the path length cannot compensate to produce detectable H I absorption. We note, that even if condensations were resolved and successfully modeled in the simulations, they would still comprise a

separate phase from the O VI absorbing gas and the H I and O VI absorbing cells would not be coincident. Thus, we caution that O VI absorption may rarely be associated with the same gas structures giving rise to H I absorption.

In Figure 7(a) we re-plot the absorption profiles. In Figures 7(c), 7(d), and 7(e) and we plot the absorbing cell hydrogen number densities, n_H, temperatures, T, and metallicities $Z/Z_\odot$ in solar units as a function of LOS velocity. What is immediately notable is that the gas phases sampled by the low-ionization ions cover a narrow range clustered around $\log n_H \simeq -2$ and $\log T \simeq 4.1$. On the other hand, there is a fairly steep metallicity gradient with LOS velocity, $\Delta \log(Z/Z_\odot)/\Delta v = -0.5/30 = -0.2$ dex (km s^{-1})$^{-1}$. Note that the velocity range over which the Mg II absorption is strongest (where the highest column density cells are selected) coincides with the lowest metallicity Mg II absorption selected cells. The relatively strong absorption is due to the slightly higher n_H and lower T values, suggesting that the ionization balance dominates the profile shape, not the metallicity. Stronger absorption *within* a profile does not necessarily suggest higher metallicity.

In contrast, the gas phases of the higher-ionization ions represent a much broader range of phases, $-4.5 \leq \log n_H \leq -1.5$ and $4.1 \leq \log T \leq 4.5$ for C IV absorption selected gas and $-5.5 \leq \log n_H \leq -3.0$ and $4.1 \leq \log T \leq 4.7$ for O VI absorption selected gas. Likewise, the metallicity ranges for these ions is quite large, $-3.0 \leq \log Z/Z_\odot \leq -1.8$. Unlike the low-ionization ions, there is no trend in these highly variable quantities with LOS velocity.

In Figure 7(f), we plot the LOS spatial locations, ΔS, of the absorption-selected cells as a function of LOS velocity. Both the H I and Mg II absorption arise in what might be considered a "cloud". By this term, we mean that the absorption arises in spatially contiguous cells over a few kiloparsec LOS pathlength and that there is little variation in the number densities and temperatures of this gas over this short pathlength [see Figures 7(c) and 7(d)].

The point here is that modeling the H I and Mg II absorption with VP decomposition, though not precisely appropriate, would not be entirely without justice. As shown in Figure 5, the VP profile model comprises two components, which reflect the velocity structure of the Mg II, C II, and Si II absorption and seems appropriate given the two clusters of low-ionization absorbing cells in LOS velocity. Furthermore, the very narrow range of cell temperatures is consistent with the isothermal assumption inherent in VP decomposition.

When we examine the physical properties of the cells selected by C IV and O VI absorption, we see an entirely different physical situation. The densities and temperatures in these cells cover a 2.5 dex and 0.5 dex range, respectively. The spatial locations are spread out on the scale of 100 kpc. Clearly, the gas selected by higher-ionization absorption profiles for this simulation do not arise in a cloud-like structure. We revisit this below.

We now compare the AOD column density and VP fitting parameters to the column densities of the absorption-selected cells. The $N_a(X^j; \Delta v)$ profiles are shown in Figure 7(b). The dotted histograms are the asymmetric $\pm 1\ \sigma$ uncertainties in each velocity pixel. The horizontal lines outside the velocity range of the detected absorption provides the upper limit on the AOD column density in the continuum of the spectra. Due to the black-bottomed saturation of the H I Lyβ absorption, the $N_a(H I; \Delta v)$ profile provides a lower limit on the column
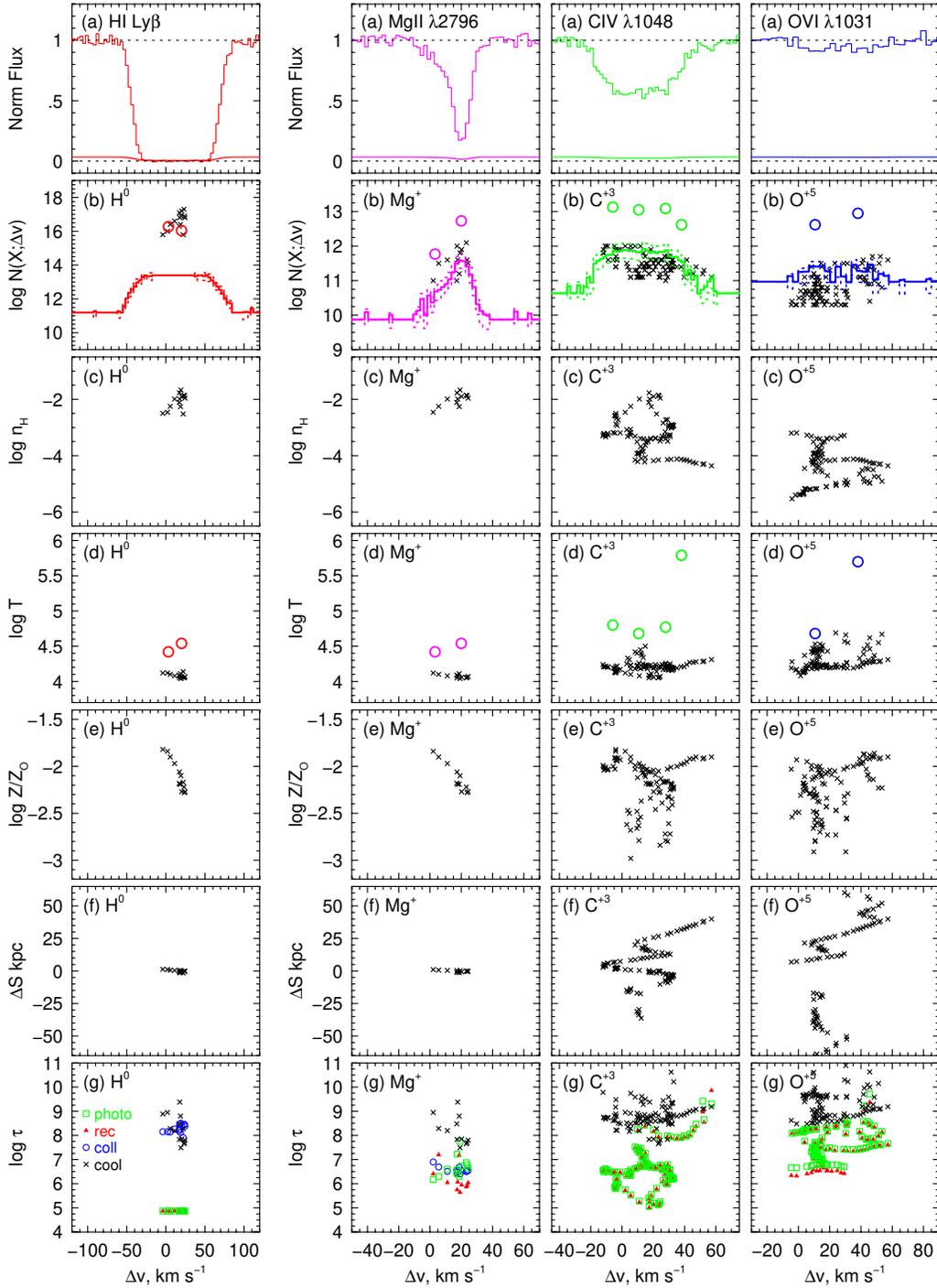
Figure 7. (from top to bottom) Absorption profiles, column densities, hydrogen densities, temperatures, spatial locations, and ionization timescales of "absorbing" cells as a function of LOS velocity for LOS 0092. (a) The absorption profiles as described in Figure 3. (b) The AOD column densities, $N_a(X; \Delta v)$, (histograms) obtained from the spectra, the absorbing cell column densities (black points), and the VP component column densities (open circles). (c) The absorbing cell hydrogen number densities, n_H. (d) The absorbing cell temperatures, T (black points) and inferred VP component temperatures (open circles; the $\times$ corresponds to the column density upper limit). (e) The absorbing cell metallicities, $\log Z/Z_\odot$. (f) The absorbing cell LOS positions, ΔS. (g) The absorbing cell photoionization (green), recombination (red), collisional (blue), and cooling timescales (black).

density in the velocity range $\Delta v \simeq \pm 40$ km s^{-1}. The individual points (black $\times$ symbols) provide the column densities of the absorption-selected cells for each transition as a function of LOS velocity.

Also shown are the VP component column densities (colored open circles; see Figure 5 for the VP model profiles and Table 1 for the VP component fitting parameters). We remind the reader that the VP models were segregated by ionization level, with H I and Mg II (along with C II and Si II) being simultaneously fit for the lower ionization phase, and C IV and O VI (along with C III) being simultaneously fit for the higher ionization phase. The low-ionization model is a two-component fit and the high-ionization model is a four component fit.

Consider the Mg II absorption. The column densities of a majority of the cells *exceed* the $N_a(\text{Mg II}; \Delta v)$ profiles. This is a fairly well understood expectation that is due to the intrinsic absorption profiles from the gas being unresolved by the spectrograph (e.g., Savage & Sembach 1991) for which correction methods have been developed (Jenkins 1996). For $\log T = 4.1$, the intrinsic absorption profile width is $\simeq 6.6$ km s^{-1} (FWHM) for Mg II, whereas the FWHM of the instrumental function for the simulated spectra is $\simeq 17$ km s^{-1}. Note that discrepancy between $N_a(X^j; \Delta v)$ and the cell column densities is also seen for the coolest gas selected by C IV and O VI absorption, since these cells give rise to the narrowest intrinsic line shapes.

The VP component column densities for the H I absorption are fairly consistent with the cell column densities, though the $\Delta v = 20$ km s^{-1} component is $\simeq 1$ dex below the dominant absorbing cells. The column densities of the Mg II VP components are also $\simeq 0.5$ dex higher than the peak column densities of the absorbing cells. If we examine the inferred temperatures of the gas from the VP components [Figure 7(d)], we see that the component temperatures are also overestimated.

Since the lower ionization profiles are decomposed into only two components, the Doppler b parameters are likely to be systematically large; that is, the kinematic morphology of the absorption is due to a steep velocity gradient across the LOS (see the Δv panels of Figure 2), which has been modeled as two thermally broadened "clouds".

For the C IV and O VI absorption, the VP component column densities and temperatures are significantly overestimated, roughly by 1.5 dex and $\simeq 0.5$ dex, respectively. In fact, the inferred temperatures from the VP components are $\log T \simeq 4.7$, and are approaching temperatures commonly assumed to be indicative of collisional ionization for these two ions (in the following subsection, we show that the C IV and O VI absorbing gas is dominated by photoionization equilibrium). The very broad component suggests $\log T \simeq 5.7$, but the VP component broadening is clearly modeling the bulk velocity flow. These considerations serve as a warning that VP decomposition can be highly misleading about the ionization condition of the gas, and may simply be a flawed approach to modeling C IV and O VI absorbing gas (as we discuss further below).

These discrepancies with the VP decomposition would undoubtedly systematically skew estimated of the gas density and metallicity inferred from ionization modeling of the VP components. However, when we examine the *total* column densities, we find good agreement between the AOD columns, $N_a(X^j)$, the VP column densities, and the absorbing cell column densities.

In Table 2, we list the total column densities for H I, Mg II,

Table 2
Comparison of Total Column Densities[a]

(1) Ion	(2) $N_{\text{tot}}(\text{VP})$ (cm^{-2})	(3) $N_{\text{tot}}(\text{AOD})$ (cm^{-2})	(4) $N_{\text{tot}}(\text{Cells})$ (cm^{-2})
H I	16.47 ± 0.10	> 14.69	17.95
Mg II	12.78 ± 0.01	$12.75^{+0.08}_{-0.06}$	12.76
C IV	13.61 ± 0.06	$13.62^{+0.05}_{-0.03}$	13.57
O VI	13.13 ± 0.42	$13.02^{+0.08}_{-0.03}$	13.03

[a] The total column densities of the absorbing gas for each analysis method, where $N_{\text{tot}}(\text{VP})$ is the sum of the individual VP component column densities, $N_{\text{tot}}(\text{AOD})$ is the integrated AOD column density given by Eq. 12, and $N_{\text{tot}}(\text{Cells})$ is the sum of the cell column densities along the LOS that contribute to the absorption profiles.

C IV, and O VI. The VP total column density is the sum of the components, the AOD total column density is given by Eq. 12, and the total for the "Cells" is the sum of the absorption selected cell column densities. That the totals are in good agreement is promising, for the consistency between observational methods for obtaining the total column densities and the actual total column density of the gas selected by absorption would imply that mass estimates of the CGM using integrated AOD profiles and summed VP column densities accurately recover the gas mass for both the low and high ionization CGM (for example, as done by Tumlinson et al. 2011; Bordoloi et al. 2014).

Interpretation of both AOD column density profiles and VP decomposition is predicated on the assumption that the absorption at a given LOS velocity arises from the same physical gas complex, or cloud. Whereas the $N_a(\text{Mg II}; \Delta v)$ profile reasonably recovers the distribution of Mg II absorbing gas column densities with LOS velocity, the same cannot be said for the gas giving rise to C IV and O VI absorption. For these ions, we see that multiple absorbing gas structures arise with virtually identical velocities and that these structures can have up to a ~ 1 dex spread in column densities. That is, the flux decrement at any given velocity can result from the sum of the column densities from multiple cells that happen to have the same LOS velocity.

When we further consider the spatial locations of absorbing cells with the same LOS velocity, we find that the assumption underlying standard observational analysis of the absorption profiles is not validated by the kinematic-spatial distribution of the absorbing gas for all ions. As mentioned above while discussing Figure 7(f), the H I absorption and the Mg II absorption is distributed over a range of velocities in gas that forms a single contiguous structure at $\Delta S \simeq 0$ (i.e., a single "cloud"). However, at most LOS velocities, the C IV and O VI absorbing gas originates from multiple groupings of cells with physical separations ranging from a few to 150 kpc.

For example, the C IV absorption in the range of $10 \leq \Delta v \leq 20$ km s^{-1} arises in six physically distinct LOS locations spread over 100 kpc with typical LOS separations of ~ 20 kpc, whereas the cells in each of these spatial groupings are contiguous over one to a few kpc. Not only does the C IV absorption arise in gas distributed over ~ 100 kpc, the gas is characterized by a complex velocity field that reverses direction along the LOS several times that results in LOS velocity caustics where the column densities of physically un-

connected gas structures are summed. The O VI absorption exhibits similar behavior. We note that in a double line-of-sight experiment, Muzahid (2014) concluded that the O VI absorption arises in large extended structures that are consistent with our simulation results. The fact that O VI and C IV arise in these extended structures with complex spatial and velocity fields is no doubt the reason that the VP component Doppler b parameters yield inferred temperatures that are ~ 1 dex too high [see Figure 7(d)].

In summary, current observational analysis techniques may be valid for low-ionization gas. As mentioned above, the H I and Mg II absorption arises in a single contiguous gas structure. The density and temperature ranges of this structure are $\log n_{\mathrm{H}} \simeq -2$ and $\log T \simeq 4.1$, respectively. Based upon standard observational techniques and Cloudy modeling applied to COS spectra, Werk et al. (2014, $L \sim L^*$ galaxies) and Stocke et al. (2013, $L > 0.1L^*$ galaxies) constrained the properties of the cool/warm photoionized CGM to reside near these values and to be generally consistent with the phase diagrams of Mg II and H I absorbing gas shown in Figure 6. However, becasue of the complex spatial-kinematic distrbution of the higher-ionization gas, current observational techniques of C IV and O VI absorption likely do *not* correctly model the underlying physics of the absorbing gas.

The implication of the kinematic-spatial distribution of the absorbing gas is that observational analysis techniques (i.e., AOD column density and/or VP decomposition coupled with ionization modeling) that are founded on the absorbing gas at a given LOS velocity arising in a physically contiguous gas structure may be quite invalid (especially for high-ionization species). It remains to be determined to what degree of accuracy the inferred densities, temperatures, and metallicites from observational modeling techniques are recovered when applied to the simulated spectra and compared to the gas cell properties. In the near future, we aim to undertake such a study (Vander Vliet et al. 2014b, in preparation).

5.3. *Ionization Equilibrium*

We now turn to the question as to whether CGM absorbing gas can be modeled with equilibrium ionization models. We also investigate methods for determining if the absorbing gas is photoionized or collisionally ionized.

Since most all ionization modeling of observational data is based upon the assumption of ionization equilibrium, it is important to understand to what degree this assumption holds. Our ionization modeling, and therefore all subsequent absorption line analysis of the simulations, is also is based upon this assumption. Investigations into non-equilibrium ionization had been investigated by Cen & Fang (2006) and by Oppenheimer & Schaye (2013). Non-equilibrium collisional ionization results in a reduction of the O VI column density relative to the equilibrium solution, though Oppenheimer & Schaye (2013) find that non-equilibrium effects are not as pronounced when photoionization is taken into account.

Whether the gas is predominantly photoionized or collisionally ionized has implications for correctly estimating the density, temperature, physical size, cooling time, and estimated mass of the absorbing gas (in otherwords, understanding the physical nature of the CGM, and subsequently its role in galaxy evolution). In observational work one cannot directly deduce whether the gas is dominated by photoionization or collisional ionization. Often, inferences of collisional iopnization are based upon the presence of large ther-

mal velocity widths in the absorption profiles, or the column density ratios of different ions in different ionization stages (e.g., Tripp et al. 2001; Simcoe et al. 2006; Tripp et al. 2011; Fox et al. 2014). However, from the ionization modeling one can directly examine the degree to which the ionization balance in the absorbing gas is dominated by photoionization or collisional ionization. The method we employ can also be applied to observational work.

The condition of ionization equilibrium is that the gas must be thermally stable over the time required for the photoionization, recombination, and collisional ionization rates to achieve a steady-state balance. If the time required to achieve ionization equilibrium is denoted τ_{eq}, the condition is often expressed,

$$\tau_{\mathrm{eq}} \ll \tau_{\mathrm{cool}} , \qquad (14)$$

where

$$\tau_{\mathrm{cool}} = \frac{Q}{|dQ/dt|} = \frac{Q}{|\Lambda_{\mathrm{net}}|} = \frac{\frac{3}{2}(n_{\mathrm{e}} + n_{\mathrm{N}})kT}{|\Lambda_{\mathrm{heat}} - \Lambda_{\mathrm{cool}}|} \quad \mathrm{sec}, \qquad (15)$$

is the cooling timescale. Here, Q is the energy density of the gas [erg cm^{-3}], n_{e} is the electron density, n_{N} is the total number density of all ions, Λ_{heat} is the heating rate per unit volume, and Λ_{cool} is the cooling rate per unit volume [erg s^{-1} cm^{-3}]. Both Λ_{heat} and Λ_{cool} are functions of the spectral energy distribution of ionizing photons, the gas density, n_{H} temperature, T, and the relative abundances of the metals.

The ionization timescales are different for each ion in the gas. As such, it is possible that some ions are in ionization equilibrium, while other ions are not. For our work, which focuses on the absorption properties of ions that are commonly observed in absorption lines studies, we aim to determine if the assumption of ionization equilibrium applies for these ions in particular.

Here, we examine three timescales, photoionization, τ^{ph}, recombination, τ^{rec}, and collisional ionization, τ^{coll}, for the four ions H^0, Mg$^+$, C^{+3} and O^{+5} in the absorption selected gas shown in Figures 2 and 7 for LOS 0092.

The ionization timescales for ion X$^{\mathrm{j}}$ are obtained by rearranging the rate equations (see Churchill et al. 2014, for full details) into the form $(1/n_{\mathrm{xj}})(dn_{\mathrm{xj}}/dt) = R_{\mathrm{xj}}$, where R_{xj} is the rate [s^{-1}] at which n_{xj} is either increasing or decreasing. The solution is of the form $e^{-t/\tau_{\mathrm{xj}}}$. Thus, the ionization timescales are the e-folding time for a change in the numder density. The rate R_{xj} is a function of the ionizing photon field, J_ν, ion densities, electron density, and gas temperature, which are all assumed to change by no more than a negligible amount so that R_{xj} can be approximated as a constant (thus, greatly simplifying the integrals; as such, the timescales are approximations). Integrating over the time interval $\tau_{\mathrm{xj}} = t_1 - t_0$ with the condition $n_{\mathrm{xj}}(t_1)/n_{\mathrm{xj}}(t_0) = e^{\pm 1}$ yields $\tau_{\mathrm{xj}} = |R_{\mathrm{xj}}|^{-1}$. The absolute value reflects the fact the change in n_{xj} may be decreasing or increasing over the time interval, but we wish to know the timescale only, regardless of the sign of dn_{xj}/dt.

Accounting only for photoionization rates (omitting Auger ionization), we obtain the photoionization timescale,

$$\tau_{\mathrm{xj}}^{\mathrm{ph}} \simeq \left| R_{\mathrm{xj}}^{\mathrm{ph}} - \frac{n_{\mathrm{xj-1}}}{n_{\mathrm{xj}}} R_{\mathrm{xj-1}}^{\mathrm{ph}} \right|^{-1} \quad \mathrm{sec}, \qquad (16)$$

where $R_{\mathrm{xj}}^{\mathrm{ph}}(J_\nu)$ is the photoionization rate [s^{-1}] for ion X$^{\mathrm{j}}$, and the density units are cm^{-3}. In the case of the neutral ion ($j =$

1), the rates indexed by $j-1$ do not enter into the derivation and are omitted from Eq. 16.

Accounting for both photo and dielectronic recombination, we obtain the recombination timescale,

$$\tau_{\mathrm{Xj}}^{\mathrm{rec}} \simeq \left| n_{\mathrm{e}} \left[\left(\beta_{\mathrm{Xj\text{-}1}}^{\mathrm{phr}} + \beta_{\mathrm{Xj\text{-}1}}^{\mathrm{die}} \right) - \frac{n_{\mathrm{Xj+1}}}{n_{\mathrm{Xj}}} \left(\beta_{\mathrm{Xj}}^{\mathrm{phr}} + \beta_{\mathrm{Xj}}^{\mathrm{die}} \right) \right] \right|^{-1} \quad \mathrm{sec}\,, \quad (17)$$

where $\beta_{\mathrm{Xj\text{-}1}}^{\mathrm{phr}}(T)$ and $\beta_{\mathrm{Xj}}^{\mathrm{die}}(T)$ are the photo and dielectronic recombination rate coefficients [cm^3 s^{-1}] for ion X$^{\mathrm{j}}$.

Accounting for both direct and excitation-auto collisional ionization processes, we obtain the collisional ionization timescale[7],

$$\tau_{\mathrm{Xj}}^{\mathrm{coll}} \simeq \left| n_{\mathrm{e}} \left[\left(\alpha_{\mathrm{Xj}}^{\mathrm{cdi}} + \alpha_{\mathrm{Xj}}^{\mathrm{cea}} \right) - \frac{n_{\mathrm{Xj\text{-}1}}}{n_{\mathrm{Xj}}} \left(\alpha_{\mathrm{Xj\text{-}1}}^{\mathrm{cdi}} + \alpha_{\mathrm{Xj\text{-}1}}^{\mathrm{cea}} \right) \right] \right|^{-1} \quad \mathrm{sec}\,, \quad (18)$$

where $\alpha_{\mathrm{Xj}}^{\mathrm{cdi}}(T)$ and $\alpha_{\mathrm{Xj}}^{\mathrm{cea}}(T)$ are the direct and excitation-auto ionization rate coefficients [cm^3 s^{-1}] for ion X$^{\mathrm{j}}$. For the derivation of Eq. 18, we have omitted charge exchange reactions.

For each cell in the simulation, we compute the energy density, Q, and the photoionization, recombination, and collisional ionization timescales directly from the photoionization rates, equilibrium electron density, and the recombination and collisional ionization rate coefficients. The computation of the rates, rate coefficients, and the equilibrium ionization condition for each gas cell is described in Churchill et al. (2014).

To compute the cooling timescale, we adopt the cooling functions of Wiersma et al. (2009). These cooling functions were generated with Cloudy 07.02 (Ferland et al. 1998) for model clouds as a function of hydrogen number density, temperature, metallicity, and redshift. The ionizing radiation is the Haardt & Madau (2001) ultraviolet background (UVB). The clouds are assumed to be dust free and optically thin. As with our ionization model, the gas is assumed to be in ionization equilibrium. We note here that it is important the cooling function accounts for photoionization processes. At a given gas density and temperature, photoionization will yield a gas that is more highly ionized than collisionally ionized gas. This results in cooling rates that are diminished as compared to the rates for collisional ionized gas (Wiersma et al. 2009; Schure et al. 2009, and references therein). Thus, the standard collisional ionization equilibrium cooling functions (e.g., Sutherland & Dopita 1993) can substantially underestimate the cooling timescales in photoionized gas.

We also note that the Wiersma et al. (2009) cooling functions are highly consistent with the cooling functions used by hydroART (Ceverino & Klypin 2009; Trujillo-Gomez et al. 2013; Ceverino et al. 2014). This is important because the cooling functions dictate the equilibrium temperature of the gas, and the gas temperature determines the collision based ionization and recombination rates in equilibrium ionization models.

The cooling functions are determined by interpolating across the high-resolution tables of Wiersma et al. (2009), which return the normalized net cooling function, $\Lambda_{\mathrm{net}}/n_{\mathrm{H}}^2$. We determined $|\Lambda_{\mathrm{net}}|$ for each gas cell in the simulation box. The cell data required for the interpolation are the hydrogen number density, n_{H}, temperature, T, redshift, z_{box} (needed for the

UVB), and the abundances of He, C, N, O, Ne, Mg, Si, S, Ca, and Fe, relative to hydrogen. The latter are detemined from the type II and Ia supernovae mass fractions in the gas cell. Note that the *individual* contributions of the aforementioned ions, based on their number densities relative to hydrogen, are accounted for in the cooling functions. We then apply Eq. 15 to compute τ_{cool} for each cell in the simulation box.

In Figure 7(g), we plot the timescales for photoionization (green open squares), recombination (red filled triangles), and collisional ionization (open blue circles) for the four ions H^0, Mg$^+$, C^{+3}, and O^{+5} in the absorption selected cells. We also plot the cooling timescales (black × symbols).

The H^0 ion is clearly in photoionization equilibrium. The photoionization and recombination timescales are equal and both of these are roughly three orders of magnitude shorter than the collisional ionization timescales. Furthermore, the cooling timescales are also roughly three orders of magnitude longer than the photoionization timescales, which satisfies the criterion given by Eq. 14 for ionization equilibrium. The collisional ionization processes of hydrogen do not achieve equilibrium, since the gas cools on similar timescales, but photoionization completely dominates the ionization of hydrogen. The Mg$^+$ ion, on the otherhand, is in near balance between photoionization, collisional ionization, and recombination. However, the assumption of ionization equilibrium is well satisfied for the majority of gas in that the cooling timescales exceed the ionization timescales.

In the cases of C^{+3} and O^{+5}, the ions are in equilibrium between the recombination and photoionization timescales. For both ions, the collisional ionization timescales exceed 100 Gyr; the gas giving rise to C IV and O VI absorption is clearly dominated by photoionization. Furthermore, the assumption of ionization equilibrium is well supported by the long cooling timescales. At LOS velocities of $\Delta v \simeq 50$ km s^{-1}, the gas may be only marginally in ionization equilibrium for these ions.

In summary, the assumption of ionization equilbrium for the commonly observed ions H^0, Mg$^+$, C^{+3}, and O^{+5} is sound for modeling the ionization conditions of the absorbing gas (at least for the CGM of this simulated galaxy). This lends a great deal of confidence that observational data can be accurately analyzed using ionization equilibrium for these ions. Futhermore, we have shown that it is straight forward to determine whether a given ion is photoionized or collisionally ionized in the absorbing gas of the simulated CGM. In principle, the method can be applied to observational data if the photoionization, collisional ionization, and recombination rate coefficients from the ionization modeling are retreivable. However, we caution that using column densities of individual VP components may not yield an ionization model that reflects the absorbing gas conditions (see Section 5.2).

6. CONCLUSIONS

We have presented a case as to why a comprehensive understanding of the CGM via absorption line studies requires objective absorption line analysis of high resolution hydrodynamic cosmological simulations that mirrors observational absorption line methods. Most importantly, we argued and demonstrated that the synthetic absorption line spectra of the simulated CGM should emulate the observed spectra in all of its characteristics, as should the analysis of the absorption line measurements obtain directly from the spectra. Primarily, this assures that the gas selected by absorption in the simulated CGM is directly comparable to the gas selected by absorption

---

[7] In some applications, the collisional timescale includes the balance with reombination. Here, we desire to know the collisional ionization timesale only. If the timescale for the balancing of recombination and ionization is desired, it can be computed from $\tau_{\mathrm{Xj}}^{\mathrm{rec}} \tau_{\mathrm{Xj}}^{\mathrm{coll}}/(\tau_{\mathrm{Xj}}^{\mathrm{rec}} + \tau_{\mathrm{Xj}}^{\mathrm{coll}})$ using Eqs. 17 and 18.

in the observed CGM. The point is that, when comparing the simulated CGM gas properties (densities, temperatures, kinematics, ionization and chemical conditions, and spatial distributions) to the properties of the CGM gas inferred from observational absorption line studies, only the gas that is selected by the simulated absorption lines should be compared. Only in this fashion are direct insights into observational analysis and the physical nature of the CGM gleaned.

We generated absorption profiles for H I the Lyα and Lyβ transitions, and for the spectra of H I Lyα and Lyβ, Si II $\lambda\lambda1190,1193$, Si II $\lambda1260$, C II $\lambda1036$ and $\lambda1335$, Mg II $\lambda\lambda2796,2803$, C IV $\lambda\lambda1548,1550$, and O VI $\lambda\lambda1031,1037$ metal-line transitions for 1000 LOS through the CGM of a simulated dwarf galaxy from the work of Trujillo-Gomez et al. (2013). Though in this paper we focused on a single LOS for illustrating the relationships between commonly observed absorption lines and the underlying properties of the absorbing gas, the results discussed for this LOS are generally true from LOS to LOS. Highlights of our findings for the CGM of this simulated galaxy are:

(1) The simulations indicate that low ionization gas, as probed in absorption with ions having ionization potentials near the hydrogen ionization edge, likely arise from what might be called "clouds". Along the LOS, these structures are characterized by a narrow range of densities and temperatures, suggesting they can be modeled as single phase structures. In addition, the absorption lines arise in gas that is localized along the LOS (the grid cells in the simulations are spatially contiguous). As such, commonly applied observational analysis methods that incorporate AOD column densities, VP decomposition, and single phase ionization modeling are likely to be sound.

(2) The simulations indicate that higher ionization gas likely arises in extended structures that sample gas distributed up to 50–100 kpc along the LOS. Furthermore, the absorption at a given LOS velocity can arise in several smaller scale regions of the gas separated by tens of kiloparsecs that circumstantially align in LOS velocity. The gas phases (densities and temperatures) that give rise to absorption at a given LOS velocity can vary up to an order of magnitude or more. As such, AOD profiles and VP decomposition do not properly reflect the high-ionization absorbing gas properties. Ionization modeling of higher ionization gas as "cloud"-like structures should be viewed with healthy skepticism. However, AOD profiles and VP decomposition can accurately reflect the total gas mass and average gas properties, because the *total* column densities from these methods are highly consistent with the total gas column along a LOS.

(3) Higher ionization gas, such as O VI absorption selected gas, can have LOS absorption velocities that overlap with the LOS absorption velocity of H I absorption selected gas, but the simulations indicate that in not all cases is the H I absorption associated with the higher ionization absorbing gas. In addition to the caveats for point (2) above, this presents further challenges for ionization modeling and metallicity estimates of the high ionization CGM.

(4) Estimates of the ionization timescales and the cooling timescales of the gas that gives rise to detected absorption indicate that the gas can be successfully modeled as being in ionization equilibrium. Broad absorption in high-ionization ions does not necessarily indicate high temperature gas that

is often taken to imply collisional ionization dominates. In fact, we found that VP decomposition of C IV and O VI absorption yielded temperatures consistent with collisional ionization when in fact the O VI absorbing gas is roughly 1 dex cooler and the broadening is due to the complexity of the spatial and velocity fields over the extended absorbing structure. Indeed, analysis of the ionization modeling showed that the C IV and O VI absorbing gas is photoionized.

To the extent that the CGM of this simulated galaxy reflects the real world, the points we have discussed here provide our first qualitative insights into the effectiveness or possible misapplication of standard absorption line analysis methods applied to studies of the CGM.

However, we have studied the simulated CGM of a single isolated low-mass (dwarf) galaxy. The star formation history is highly stochastic and "bursty" (Trujillo-Gomez et al. 2013), and there are no satellite galaxies and filamentary accretion is negligible. The effects of both these characteristics are certainly manifest in the global CGM properties of this simulated galaxy. It remains to be seen if the CGM of higher mass galaxies in more complex cosmological environments presents a substantially different or broader set of insights.

In the future, we aim to undertake a comprehensive quantitative analysis of the simulated CGM, comparing the inferences derived from various observational works to the inferences derived from the application of observational analysis methods to simulated absorption data. Examples of observational data that can be compared are the covering fractions, the column density and equivalent width impact parameter distributions, and the kinematics. In particular, these quantities may promise to provide insight into how the CGM properties reflect different stellar feedback recipes.

Using the absorption selected gas properties, we aim to also quantify the degree to which the observational analysis methods accurately recover the "true" properties of absorbing gas. We aim to determined to what degree of accuracy the inferred densities, temperatures, and metallicities from observational modeling techniques are recovered when applied to the simulated spectra and compared to the gas properties. This work will require full application of the AOD column density, VP decomposition, and ionization modeling techniques. It is also an immediate goal to include and test shielding and basic radiative transfer effects in our ionization model (Churchill et al. 2014) so that we can relax the optically thin constraint.

REFERENCES

Agertz, O., & Kravtsov, A. V. 2014, arXiv:1404.2613
Agertz, O., Kravtsov, A. V., Leitner, S. N., & Gnedin, N. Y. 2013, ApJ, 770, 25
Behroozi, P. S., Conroy, C., & Wechsler, R. H. 2010, ApJ, 717, 379
Behroozi, P. S., Wechsler, R. H., & Conroy, C. 2013, ApJ, 770, 57

Boksenberg, A., Carswell, R. F., & Sargent, W. L. W. 1979, ApJ, 227, 370
Bordoloi, R., Lilly, S. J., Knobel, C., et al. 2011, ApJ, 743, 10
Bordoloi, R., Tumlinson, J., Werk, J. K., et al. 2014, arXiv:1406.0509
Bouché, N., Hohensee, W., Vargas, R., et al. 2012, MNRAS, 426, 801
Cen, R., & Fang, T. 2006, ApJ, 650, 573
Ceverino, D., Dekel, A., & Bournaud, F. 2010, MNRAS, 404, 2151
Ceverino, D., Dekel, A., Tweed, D., & Primack, J. 2014, arXiv:1409.2622
Ceverino, D., & Klypin, A. 2009, ApJ, 695, 292
Ceverino, D., Klypin, A., Klimek, E., et al. 2013, MNRAS, 442, 1545
Chabrier, G. 2003, PASP, 115, 763
Charlton, J. C., Ding, J., Zonak, S. G., et al. 2003, ApJ, 589, 111
Churchill, C. W. 1997, Ph.D. Thesis, University of California, Santa Cruz
Churchill, C. W., & Charlton, J. C. 1999, AJ, 118, 59
Churchill, C. W., Kacprzak, G. G., Steidel, C. C., et al. 2012, ApJ, 760, 68
Churchill, C. W., Klimek, E., Medina, A., & Vander Vliet, J. R. 2014, ApJ, submitted
Churchill, C. W., Mellon, R. R., Charlton, J. C., Jannuzi, B. T., Kirhakos, S., Steidel, C. C., & Schneider, D. P. 2000, ApJS, 130, 91
Churchill, C. W., Mellon, R. R., Charlton, J. C., & Vogt, S. S. 2003a, ApJ, 593, 203
Churchill, C. W., Rigby, J. R., Charlton, J. C., & Vogt, S. S. 1999, ApJS, 120, 51
Churchill, C. W., & Vogt, S. S. 2001, AJ, 122, 679
Churchill, C. W., Vogt, S. S., & Charlton, J. C. 2003b, AJ, 125, 98
Crighton, N. H. M., Hennawi, J. F., Simcoe, R. A., et al. 2014, arXiv:1406.4239
Davis, S. W., Jiang, Y.-F., Stone, J. M., & Murray, N. 2014, arXiv:1403.1874
Ding, J., Charlton, J. C., Churchill, C. W., & Palma, C. 2003, ApJ, 590, 746
Evans, J. L. 2008, Ph.D., New Mexico State University, http://astronomy.nmsu.edu/jlevans/dissertation/
Evans, J. L., Churchill, C. W., Murphy, M. T., Nielsen, N. M., & Klimek, E. S. 2013, ApJ, 768, 3
Ferland, G. J., Korista, K. T., Verner, D. A., et al. 1998, PASP, 110, 761
Ferland, G. J., Porter, R. L., van Hoof, P. A. M., et al. 2013, RMxAA, 49, 137
Ford, A. B., Davé, R., Oppenheimer, B. D., et al. 2013a, arXiv:1309.5951
Ford, A. B., Oppenheimer, B. D., Davé, R., et al. 2013b, MNRAS, 432, 89
Fox, A. J., Ledoux, C., Petitjean, P., & Srianand, R. 2007b, A&A, 473, 791
Fox, A. J., Petitjean, P., Ledoux, C., & Srianand, R. 2007a, A&A, 465, 171
Fox, A. J., Wakker, B. P., Barger, K. A., et al. 2014, ApJ, 787, 147
Haardt, F., & Madau, P. 2001, in Clusters of Galaxies and the High Redshift Universe Observed in X-rays, XXIst Moriond Astrophysica Meeting, eds. D. M. Neumann & J. T. V. Tran, 64
Haardt, F., & Madau, P. 2011, ApJ, arXiv:1105.2039
Hopkins, P. F., Quataert, E., & Murray, N. 2011, MNRAS, 417, 950
Humlíček, J. 1979, Journal of Quantitative and Radiative Transfer, 21, 309
Hummels, C. B., Bryan, G. L., Smith, B. D., & Turk, M. J. 2013, MNRAS, 430, 1548
Jenkins, E. B. 1996, ApJ, 471, 292
Kacprzak, G. G., Churchill, C. W., & Nielsen, N. M. 2012, ApJ, 760, L7
Kacprzak, G. G., Churchill, C. W., Steidel, C. C., Spitler, L. R., & Holtzman, J. A. 2012, MNRAS, 427, 3029

Klypin, A., Kravtsov, A. V., Bullock, J. S., & Primack, J. R. 2001, ApJ, 554, 903
Kravtsov, A. V. 1999, Ph.D. Thesis, New Mexico State University
Kravtsov, A. V., Gnedin, O. Y., & Klypin, A. A. 2004, ApJ, 609, 482
Kravtsov, A. V., & Klypin, A. A. 1999, ApJ, 520, 437
Kravtsov, A. V., Klypin, A. A., & Khokhlov, A. M. 1997, ApJS, 111, 73
Kriss, G. A. 2011, Improved Medium Resolution Line Spread Functions for COS FUV Spectra, COS ISR 2011-01(v1), (Baltimore, STScI)
Krumholz, M. R., & Tan, J. C. 2007, ApJ, 654, 304
Krumholz, M. R., & Thompson, T. A. 2012, ApJ, 760, 155
Lanzetta, K. M., Bowen, D. V., Tytler, D., & Webb, J. K. 1995, ApJ, 442, 538
Lehner, N., Howk, J. C., Tripp, T. M., et al. 2013, ApJ, 770, 138
Leitherer, C., Schaerer, D., Goldader, J. D., et al. 1999, ApJS, 123, 3
Lopez, L. A., Krumholz, M. R., Bolatto, A. D., et al. 2013 ApJ, 795, 121
Mathes, N. L., Churchill, C. W., Kacprzak, G. G., et al. 2014, arXiv:1406.2314
More, J. J. in Numerical Analysis Proceedings, ed. G. A. Watson, Lecture Notes in Mathematics (Springer-Verlag), 630
Moster, B. P., Naab, T., & White, S. D. M. 2013, MNRAS, 428, 3121
Munshi, F., Governato, F., Brooks, A. M., et al. 2013, ApJ, 766, 56
Murray, N., & Rahman, M. 2010, ApJ, 709, 424
Muzahid, S. 2014, ApJ, 784, 5
Nielsen, N. M., Churchill, C. W., & Kacprzak, G. G. 2013b, ApJ, 776, 115
Nielsen, N. M., Churchill, C. W., Kacprzak, G. G., & Murphy, M. T. 2013a, ApJ, 776, 114
Oppenheimer, B. D., & Davé, R. 2008, MNRAS, 387, 577
Oppenheimer, B. D., & Davé, R. 2009, MNRAS, 395, 1875
Oppenheimer, B. D., Davé, R., Kereš, D., et al. 2010, MNRAS, 406, 2325
Oppenheimer, B. D., & Schaye, J. 2013, MNRAS, 434, 1043
Savage, B. D., & Sembach, K. R. 1991, ApJ, 379, 245
Schneider, D. P., et al. 1993, ApJS, 87, 45
Schure, K. M., Kosenko, D., Kaastra, J. S., Keppens, R., & Vink, J. 2009, A&A, 508, 751
Sembach, K. R., & Savage, B. D. 1992, ApJS, 83, 147
Simcoe, R. A., Sargent, W. L. W., Rauch, M., & Becker, G. 2006, ApJ, 637, 648
Stocke, J. T., Keeney, B. A., Danforth, C. W., et al. 2013, ApJ, 763, 148
Stocke, J. T., Penton, S. V., Danforth, C. W., Shull, J. M., Tumlinson, J., & McLin, K. M. 2006, ApJ, 641, 217
Sutherland, R. S., & Dopita, M. A. 1993, ApJS, 88, 253
Tripp, T. M., Giroux, M. L., Stocke, J. T., Tumlinson, J., & Oegerle, W. R. 2001, ApJ, 563, 724
Tripp, T. M., Meiring, J. D., Prochaska, J. X., et al. 2011, Science, 334, 952
Trujillo-Gomez, S., Klypin, A., Colin, P., et al. 2013, arXiv:1311.2910
Tumlinson, J., Thom, C., Werk, J. K., et al. 2011, Science, 334, 948
Tumlinson, J., Thom, C., Werk, J. K., et al. 2013, ApJ, 777, 59
van de Voort, F., & Schaye, J. 2012, MNRAS, 423, 2991
Werk, J. K., Prochaska, J. X., Tumlinson, J., et al. 2014, arXiv:1403.0947
Wiersma, R. P. C., Schaye, J., & Smith, B. D. 2009, MNRAS, 393, 99